Modeling nanoelectromechanical resonator signals for experimental mass measurements : a Total Variation formulation

T. Fortin, A. Reynaud, S. Jeudy, S-H. Lai, V. Çumaku, C. Abergel, S. Hentz, C. Masselon

IEEE Access
Multidisciplinary | Rapid Review | Open Access Journal

Date of publication xxxx 00, 0000, date of current version xxxx 00, 0000.

Digital Object Identifier

Modeling nanoelectromechanical resonator signals for experimental mass measurements : a Total Variation formulation

T. FORTIN[1], A. REYNAUD[2], S. JEUDY[3], S-H. LAI[1], V. ÇUMAKU[1], C. ABERGEL[3], S. HENTZ[2] and C. MASSELON[1]

[1]EDyP Laboratory, Univ. Grenoble Alpes, CEA, Inserm, IRIG, BGE UA13, 17 avenue des martyrs, 38000 Grenoble, France
[2]University of Grenoble Alpes, CEA, LETI, 17 avenue des martyrs, 38 000 Grenoble, France
[3]Aix–Marseille University, Centre National de la Recherche Scientifique, Information Génomique Structurale, Unité Mixte de Recherche 7256 (Institut de Microbiologie de la Méditerranée, FR3479, IM2B, IOM), 13288 Marseille Cedex 9, France.

Corresponding author: T. Fortin (e-mail: thomas.fortin@cea.fr).

This work was funded by the Cross-Disciplinary Program on Instrumentation and Detection of the French Alternative Energies and Atomic Energy Commission [CEA](VIA-NEMS) and VÇ's thesis fellowship was funded by the Grenoble Alliance for Integrated Structural and Cell Biology, a program of the Chemistry Biology Health Graduate School, University Grenoble Alpes (ANR-17-EURE-0003).

ABSTRACT Nanoelectromechanical resonators (NEMS) have recently emerged as mass measurement devices with interesting potential, and with mass ranges hardly covered by conventional techniques, they offer the possibility of studying intact nanoparticles, whether artificial or biological. However, different physical phenomena perturb the NEMS signals, lowering the mass accuracy and resolution of our devices. In a previous report, we thus proposed a model to remove colored noise affecting NEMS signals: Through a total variation formulation, noisy NEMS signals are "projected" onto the space of piecewise constant functions, to which non-noisy NEMS signals should theoretically belong. For the simulated NEMS signals, we obtained better mass accuracy and resolution than a commonly used reference method. However, this first model is not adapted to handle true experimental NEMS signals because, in the latter, we observe piecewise linear structures in addition to noise effects. As these unexpected structures, which we refer to as "drifts", perturb NEMS signals and consequently mass measurements, we propose a new denoising model that takes into account both noise and drift effects under any experimental conditions. This model shows increased mass accuracy and resolution, improved signal-to-noise ratio compared to a commonly used reference method, and is robust enough to handle data from experimental measurements. Moreover, as the quantification of drift features becomes accessible, we develop a scenario about the origin of the drifts and compare it with our experimental results.

INDEX TERMS Drifts, particles mass measurements, proximal methods, nanoelectromechanical resonator, nonlinear coupling, resonance frequency denoising, total variation algorithm.

I. INTRODUCTION

Nanoelectromechanical resonators (NEMS) are attracting growing interest in the mass spectrometry community [1]-[5], and are capable of measuring particle mass in the range 10^6-10^9 dalton (Da), which is hardly reached by conventional mass spectrometers, with a mass-independent resolution [6], [7]. These properties allow the measurement of the mass of intact biological particles, which is particularly interesting in viral studies to assess genome packaging [1], [8].

Measuring the masses of particles with a NEMS relies on measuring the downwards shifts in the NEMS resonance frequencies owing to the accretion of these particles on its surface. Because NEMS resonance frequencies depend mainly on the resonator's mass and because accretion of a particle increases this mass, NEMS resonance frequencies suddenly decrease upon particle landing and stabilize to new values, between particle deposition. In short, it is sufficient to record NEMS resonance frequencies over time and then identify and quantify frequency downshifts to estimate the mass of a particle population. Nevertheless, with the NEMS geometry considered herein (a doubly clamped beam), there is no one-to-one mapping between the mass value of a single particle and the downshift value of a single resonance frequency. For

such a NEMS configuration, the authors in [6] showed that the downshift of a single resonance frequency depends not only on the mass of the accreted particle, but also on the particle landing position on the NEMS. A solution to this difficulty was proposed in [6] by relating the mass and position of a particle to the downshifts of two resonance frequencies using the following system of nonlinear coupled equations:

$$\begin{aligned} \frac{\mathbf{s}^1(t+\Delta t)-\mathbf{s}^1(t)}{\mathbf{s}^1(t)} &:= \frac{m}{M}\Phi^1(x) \\ \frac{\mathbf{s}^2(t+\Delta t)-\mathbf{s}^2(t)}{\mathbf{s}^2(t)} &:= \frac{\mathbf{s}^1(t+\Delta t)-\mathbf{s}^1(t)}{\mathbf{s}^1(t)}\Phi(x) \end{aligned} \tag{1}$$

where $\mathbf{s}^i$ for $i = 1, 2$ is the i^{th} resonance frequency, t is the particle deposition time, $t + \Delta t$ is a time immediately following the particle deposition time, m is the particle mass, M is the mass of the resonator, x is the particle landing position on the resonator, and Φ^1, Φ are known bounded nonlinear functions corresponding to the shapes of the resonator's vibration modes (see [6] for detailed expressions).

Nevertheless, System (1) is derived from a model that considers NEMS physics, but neglects all external phenomena that could interfere with NEMS oscillations, and as a by-product, could affect particle mass measurements. Thus, the noise naturally affecting experimental NEMS resonance frequencies [9] is not taken into account, whereas it has a non-negligible effect on the particle mass derived from (1): By making identification and precise measures of resonance frequency downshifts more difficult, noise leads to a loss in mass accuracy and mass resolution in experiments. The problem of loss in mass accuracy and resolution in the presence of noise was addressed in [10], where a denoising model based on a nonlinear total variation formulation is described. This model "projects" noisy NEMS signals onto the space of piecewise constant functions, a space to which non-noisy NEMS signals should theoretically belong. As a result, this model shows promising results in terms of both mass accuracy and resolution when applied to simulated signals. However, System (1) and the aforementioned model do not account for experimental phenomena that alter the resonance frequency behavior. If the resonance frequencies seen as time functions should theoretically be piecewise constant functions (every discontinuity corresponding to a single particle deposition), Figure 1 shows that they can actually exhibit more complex time-dependent behavior during experimental measurements.

To the best of our knowledge, these time structures have not been reported previously. Consequently, there have been no explanations for their existence or evaluations of their impact on particle mass measurements. It seems interesting to model these structures (we call "drifts") according to these two objectives. Thus, we propose a new denoising model for NEMS resonance frequencies that captures the real complexity of drifts affecting these traces while preserving the particle mass accuracy and resolution. As a by-product, our model provides direct access to a simple drift description, creating a new tool that could be used in future developments to relate these phenomena.

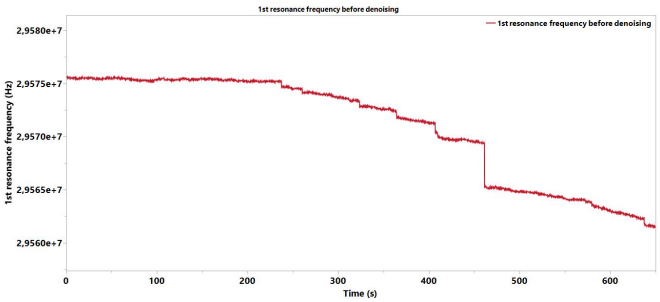

FIGURE 1. First resonance frequency trace from experiments between 0s and 650s. Observe that this trace cannot be modeled by a piecewise constant function over time, but instead requires the addition of frequency drifts between discontinuities

II. OUTLINE

After introducing the mathematical notations required to define our model, we present the scientific context on which we rely. This includes previous studies on NEMS signal denoising, as well as the mass measurement device we currently use for our experiments. This brief description enables us to introduce and define the main structures that constitute the NEMS resonance frequency trace. With these definitions, we propose a model of these structures in accordance with our experimental observations and describe the adapted detection methods. We then show how we improve the algorithm presented in [10] by considering both drift modeling and the need for accurate mass estimates; in particular, we present the different minimization problems we use to this aim and their different properties. Finally, we confront our model with experimental mass measurements and compare its performance with that of a reference method.

III. NOTATIONS

Because this study is a direct extension of that conducted in [10], we use similar notations. Our goal is to provide a unified system of notations to ease reading and emphasize the continuity between articles.

A. ALGEBRAIC NOTATIONS

We assume that all the matrices and vectors are real. A bold capital letter denotes a matrix and a bold lower-case letter denotes a column vector. A lower-case Greek letter denotes a scalar.

The space of real matrices with n rows and m columns is denoted $\mathbb{R}^{n\times m}$ and the space of column vectors with n rows is denoted $\mathbb{R}^n$. Superscript $\top$ used with a matrix or vector denotes the transposed matrix or vector. When the negative operator precedes $\top$ symbol, it refers to the inverse of the corresponding transposed matrix. Following this notation, superscript -1 used with a matrix denotes the inverse matrix if it exists. The coefficient at line i and column j of any matrix

$\mathbf{A}$ is denoted $\mathbf{A}_{ij}$. Similar notation is used when dealing with vectors. The Euclidean dot-product and norm for vectors are denoted $\langle ., . \rangle_2$ and $||.||_2$, respectively. Similarly, the L^1 norm for vectors is denoted $||.||_1$.

Some letters or symbols are reserved for specific scalars, vectors, and matrices. Thus, δ_{ij} for any positive integers i and j denotes the Kronecker symbol: $\delta_{ij} = 1$ if $i = j$ and $\delta_{ij} = 0$ if $i \neq j$. For a given integer n, $\mathbf{1}_n$ and $\mathbf{0}_n$ denote a vector in $\mathbb{R}^n$ whose components are equal to 1 and 0, respectively. The square identity matrix of size n is denoted $\mathbf{Id}_n$. Matrices $\mathbf{V}^i$ $i = 1, 2$ are the denoising matrices associated with the i^{th} resonance frequency $\mathbf{f}_i$ and they are supposed to be invertible. ∇ is the gradient operator that maps a vector of $\mathbb{R}^n$ onto $\mathbb{R}^{n-1}$:

$$(\nabla \mathbf{s})_i := \mathbf{s}_{i+1} - \mathbf{s}_i \quad i = 1, \ldots, n-1, \quad \mathbf{s} \in \mathbb{R}^n$$

By extension, for any vector $\mathbf{v} \in \mathbb{R}^n$, we will note $\nabla \mathbf{v} \in \mathbb{R}^{n-1}$ the vector whose the i^{th} component is equal to $(\nabla \mathbf{v})_i$ for $i = 1, \ldots, n-1$.

B. MODEL NOTATIONS

Let $T > 0$ be a real number and F be a set of N ordered and equally spaced real numbers in the interval $[0, T]$. It is assumed that the first element of F is zero and the last element is equal to T. An element of F is denoted f_i with $i = 1, \ldots, N$ and we assume that F is ordered in ascending order: If $1 \leq i \leq j \leq N$ then $f_i \leq f_j$. Consequently, F is equivalently represented by the set $[1, \ldots, N]$ (the set of the N first non-zero integers), through the one-to-one mapping t which verifies $t(f_i) = i$.

For any integer $k \geq 0$, $\mathcal{P}_k$ denote the space of polynomials of degree k. For any subset $G \subset F$, we note $\mathcal{C}^1_G$ the space of real continuous functions on $[0, T]$ that are also differentiable everywhere except perhaps on G.

Let now consider two ordered sets $J^0 \subset J^1 \subset F$ such that if $f_i \in F \cap J^0$ then $f_{i+1} \in J^1 - J^0$. We also assume that f_1 and f_N do not belong to J^1. Without any restriction, both J^0 and J^1 can be equal to the empty set $\emptyset$ if required. Once J^0 and J^1 are defined, we introduce the following functions spaces (for $k = 0, 1$):

$$\mathcal{V}^1 := \{\mathbf{v} \in \mathcal{C}^1_{J^1} \times \mathcal{C}^1_{J^1} \mid \mathbf{v}|_{[f_i, f_{j+1}]} \in \mathbb{P}_1 \times \mathbb{P}_1, \ \forall f_j \in F\}$$
$$\mathcal{V}^0 := \{\mathbf{v} \in \mathcal{V}^1 \mid \mathbf{v}(f_j) = \mathbf{v}(f_{j+1}), \ \forall f_j \in F - J^0\}$$
$$\mathcal{D}^k := \{\mathbf{v} \in \mathcal{V}^k \mid \mathbf{v}^i(f_{j+1}) \leq \mathbf{v}^i(f_j), \ \forall f_j \in F \cap J^0, \ i = 1, 2\}$$

With the above definitions, we have $\mathcal{V}^0 \subset \mathcal{V}^1$ and $\mathcal{D}^0 \subset \mathcal{D}^1$. Moreover, we observe that every function of these spaces is completely defined when its values on set F are known, which means that $\mathcal{V}^k$ and $\mathcal{D}^k$ for $k = 0, 1$ can be equivalently represented by some subsets of $\mathbb{M} := \mathbb{R}^N \times \mathbb{R}^N$. If we denote $\mathbb{V}^k = t(\mathcal{V}^k)$ and $\mathbb{J}^k = t(\mathcal{J}^k)$ for $k = 0, 1$, we obtain:

$$\mathbb{V}^1 := \{\mathbf{v} \in \mathbb{M} \mid (\nabla \mathbf{v})_j = (\nabla \mathbf{v})_{j-1}, \ \forall j \notin \mathbb{J}^1\}$$
$$\mathbb{V}^0 := \{\mathbf{v} \in \mathbb{V}^1 \mid (\nabla \mathbf{v})_j = 0, \ \forall j \notin \mathbb{J}^0\}$$
$$\mathbb{D}^k := \{\mathbf{v} \in \mathbb{V}^k \mid \mathbf{v}^i_{j+1} \leq \mathbf{v}^i_j, \ \forall j \in \mathbb{J}^0, \ i = 1, 2\}$$

Similarly to the case of function spaces, we have the following inclusion rules: $\mathbb{V}^0 \subset \mathbb{V}^1$ and $\mathbb{D}^0 \subset \mathbb{D}^1$. It is then equivalent to considering a function of $\mathcal{V}^k$ (respectively $\mathcal{D}^k$) $k = 0, 1$ or a vector of $\mathbb{V}^k$ (resp. $\mathbb{D}^k$).

It is also straightforward to see that the spaces $\mathbb{V}^k$ for $k = 1, 2$ are finite-dimensional vector spaces. Thus, $\mathbb{V}^0$ has dimension $n_0 := 2(1 + |J^0|)$, where $|J^0|$ is the size of J^0 and similarly, $\mathbb{V}^1$ has dimension $n_1 := 2(2 + |J^1|)$, where $|J^1|$ stands for the size of J^1. Based on this observation, we deduce that there are linear mappings $\mathbf{G}_k$ for $k = 0, 1$ between $\mathbf{s} \in \mathbb{V}^k$ and a vector in $\mathbb{R}^{n_k}$. Each mapping $\mathbf{G}_k$ is characterized by components that are equal to $\mathbf{s}_1$ and $(\nabla \mathbf{s})_i$ (plus $(\nabla \mathbf{s})_1$ if $k = 1$) for $i \in J^k$ because we have:

$$\mathbf{s}_j = \mathbf{s}_1 + \sum_{k=1}^{j-1} (\nabla \mathbf{s})_k \quad \forall j \in [1, \ldots, N]$$

These mappings $\mathbf{G}_k$ for $k = 0, 1$ are injective matrices and belong to $\mathbb{R}^{N \times n_k}$. Consequently, for a vector $\mathbf{s} \in \mathbb{V}^k$ there is a unique vector $\mathbf{r} \in \mathbb{R}^{n_k}$ such that the relation $\mathbf{s} = \mathbf{G}_k \mathbf{r}$ holds. The vector $\mathbf{r}$ is called the "gradient-like" vector of $\mathbf{s}$ and is denoted as $\mathbf{g}(\mathbf{s})$.

The set of all "gradient-like" vectors for elements in $\mathbb{D}^k \subset \mathbb{V}^k$ for $k = 0, 1$ is denoted $\mathbb{G}^k$ and has the following definition:

$$\mathbb{G}^k := \{\mathbf{v} \in \mathbb{R}^{n_k} \mid \mathbf{v}_i \leq 0 \quad \forall i \in \mathbb{J}^0\}$$

After the definition of $\mathbb{G}^k$ $k = 0, 1$, we introduce diagonal matrices $\mathbf{J}^k \in \mathbb{R}^{n_k \times n_k}$ that select the components of a "gradient-like" vector $\mathbf{g}(\mathbf{s}) \in \mathbb{G}^k$ corresponding to an index in $\mathbb{J}^k$ for the vector $\mathbf{s}$. Similarly, we denote $\mathbf{D}_k = \mathbf{Id}_{n_k} - \mathbf{J}^k$ as the diagonal matrices in $\mathbb{R}^{n_k \times n_k}$ which select the components of $\mathbf{g}(\mathbf{s})$ not corresponding to an index in $\mathbb{J}^k$ for $\mathbf{s}$. These sets of indices are denoted $\mathbb{I}_{\mathbb{G}^k}$ for $k = 0, 1$. In some cases, two "gradient-like" vectors $\mathbf{g}(\mathbf{s})$ and $\mathbf{g}(\mathbf{u})$ in $\mathbb{G}^k$ may be related to a linear relation of the form $\mathbf{J}^0 \mathbf{g}(\mathbf{s}) = \mathbf{\Phi} \mathbf{J}^0 \mathbf{g}(\mathbf{u})$, where $\mathbf{\Phi} \in \mathbb{R}^{n_k \times n_k}$ is a diagonal matrix. The coefficients of matrix $\mathbf{\Phi}$ are all equal to zero except for the diagonal coefficients of index i such that $(\mathbf{J}^0 \mathbf{g}(\mathbf{u}))_i \neq 0$. In the latter case, $\mathbf{\Phi}_{ii} = \alpha_i$ where α_i is a positive real number in an interval $[0, \phi_i]$, with upper bound ϕ_i being a known function of the sole index i. The space of this type of matrix is denoted $\mathbb{H}$.

Finally, we introduce the diagonal matrix $\mathbf{L}^k \in \mathbb{R}^{N-1 \times n_k}$ $k = 0, 1$ which ensures that the L^1 norm of $\nabla \mathbf{s}$ for $\mathbf{s} \in \mathbb{V}^k$ is equal to the L^1 norm of its gradient-like vector $\mathbf{g}(\mathbf{s})$:

$$||\nabla \mathbf{s}|| = ||\mathbf{L}^k \mathbf{g}(\mathbf{s})||_1$$

IV. SCIENTIFIC CONTEXT

The problem of loss of mass accuracy and mass resolution owing to noise was addressed in [10], where we proposed a process to estimate non-noisy resonance frequency traces from experimental measurements. This process is based on

denoising experimental traces of the first two resonance frequencies through a specific adaptation of the Total Variation (TV) minimization approaches [11], [12]:

$$\left(\hat{\mathbf{s}}^1, \hat{\mathbf{s}}^2\right) := \underset{\substack{\left(\mathbf{v}^1, \mathbf{v}^2\right) \in \mathbb{D}^0 \times \mathbb{D}^0 \\ \nabla \mathbf{v}^2 = \mathbf{\Phi}\ \nabla \mathbf{v}^1,\ \mathbf{\Phi} \in \mathbb{H}}}{\arg\min} F_1\left(\mathbf{v}^1\right) + F_2\left(\mathbf{v}^2\right) \quad (2)$$

Where the functionals F_i $i = 1, 2$ are defined as:

$$F_i\left(\mathbf{v}^i\right) := ||\nabla \mathbf{v}^i||_1 + \frac{\lambda_i}{2} ||\mathbf{V}^i(\mathbf{v}^i - \mathbf{f}^i)||_2^2$$

We claimed that the formulation above is well adapted to yield accurate denoised estimates of experimental resonance frequency traces and, consequently, good estimates of particle mass. The argument relies on the fact that (2) incorporates as much NEMS physics as is available. Thus, $\mathbb{D}^0$ represents the space of the piecewise constant functions, a space to which the resonance frequency traces should theoretically belong. Similarly, the imposed constraint $\nabla \mathbf{v}^2 = \mathbf{\Phi}\ \nabla \mathbf{v}^1$ is the mirror image of (1), which theoretically relates to the downshifts of the first two resonance frequencies. Finally, the parameters λ_i and operators $\mathbf{V}_i$, $i = 1, 2$ reflect the noise structure, which affects the resonance frequencies. However, (2) provides an additional property that stems from TV formulation. Through the L^1 term, it controls the spread of resonance frequency downshift amplitudes, and consequently, controls the sharpness of the particle mass distribution.

Problem (2) eventually shows promising denoising capabilities, which in turn induce a non-negligible gain in particle mass resolution [10]. However, because it is designed for piecewise constant functions, Problem (2) appears to be poorly suited to experimental data that show time-dependent behavior, as shown in Figure 1. These structures may find their origins in the NEMS interaction with its surrounding environment, comprising our NEMS mass spectrometer system as a whole (see Figure 2 and [13] for technical details) as well as the experimental physical conditions (ambient pressure, temperature, etc.). Consequently, these structures may carry interesting additional information, and we propose a model to access this information.

V. IDENTIFYING TRACE FEATURES

In this section, we propose a classification of the different structures that appear in experimental resonance frequency traces. Once defined, this nomenclature enables us to propose a model for each of the identified structures. Finally, we focus on methods that discriminate between these structures one from another.

A. TRACE FEATURES MODELING

As shown in Figure 1, we identify two types of structures in the NEMS resonance frequency trace. The most apparent structures are the sharp frequency downshifts that happen from time to time. These downshifts occur almost instantaneously and appear simultaneously in the first two resonance frequencies. These criteria are typical markers of particle

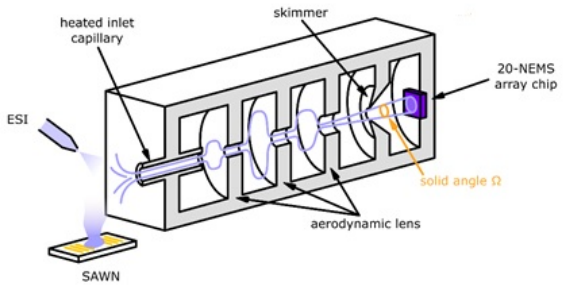

FIGURE 2. Simplified schematic of the nanomechanical mass spectrometer. (a) SAWN or Nano-ESI : Nebulization systems to aerosolize solvated particles. (b) Heated capillary: System to remove residual solvent from aerosolized particles. (c) Vacuum chambers: Systems driving aerosolized particles towards the NEMS thanks to pressure gradients mechanisms. (d) Focusing lens: System to concentrate the aerosolized particles into a narrow beam. (d) NEMS array: System of 20 independent NEMS where aerosolized particles accrete. Adapted from "'Compact and Modular System Architecture for a Nano-Resonator-Mass Spectrometer," by A. Reynaud *et al., Frontiers in Chemistry,* vol. 11, 2023.

deposition. The other structures are located between those identified as particle deposition events. These portions of frequency traces appear as slowly decreasing functions with continuous but complex shapes, and seem to have a weak correlation in the first and second resonance frequencies. Since these structures also exhibit a long-term trend, we refer to them as "drifts", while particle deposition events are referred to as "discontinuities". These denominations are used throughout the remainder of this report.

As mentioned above, a particle deposition event induces an increase in the NEMS mass, causing downshifts in the first two resonance frequencies. If the latter were recorded continuously, these downshifts would be instantaneous and appear as discontinuities (hence, the term) in the frequency traces. Because the frequencies are only sampled in our experimental process, these discontinuities in traces appear simultaneously in the first two resonance frequencies as steep straight lines between two consecutive time points. However, these features cannot be considered to be unequivocal. Because noise affects NEMS resonance frequencies, random frequency downshifts with the same characteristics may occur with a certain probability. To distinguish these random events from the true particle depositions, we need to add a supplementary condition. Thus, a simultaneous decrease in the resonance frequency traces can be associated with true particle deposition if the probability of being generated solely by pure noise effects is low.

Following the description above, a "drift" is a continuous portion of a frequency trace that does not contain a trace discontinuity. Because discontinuities occur simultaneously in the first two resonance frequencies, drifts also begin and

end simultaneously for both frequencies. To the best of our knowledge, these trends have not been linked to a specific physical phenomenon in the context of individual particle mass measurements and have no clear explanations. Thus, to obtain an idea of what could cause these trends, we propose a model that captures what can be observed in experimental measurements.

In the case of sampled resonance frequency traces, we modeled drifts as trace portions containing at least three successive time points. Such a criterion is the minimum to differentiate a drift from a discontinuity; however, drifts are usually constituted by more than three time points. To transcribe the idea of a complex but continuous shape, we then modeled every drift as a piecewise linear continuous function. This modeling allows a large flexibility in drift representation, because a single drift can be represented by a single linear polynomial as well as by a set of several contiguous linear polynomials, thus allowing the capture of details at time scales smaller than the drift duration. Moreover, selecting linear polynomials as the basic components is the most optimal choice because the minimum size of the drift is three points. With higher degree polynomials, we could overfit the resonance frequency traces in the worst cases and conversely, choosing constant polynomials would lead to either discontinuous or constant drifts, in contrast to what the experimental data seem to show.

The previous considerations enabled us to define appropriate mathematical structures relevant to modeling resonance frequency traces. Thus, a frequency trace is represented by a function that belongs to space $\mathcal{D}^1$, or equivalently by a vector that belongs to $\mathbb{D}^1$. The starting locations of the discontinuities are the indices in J^0, and because traces are continuous but non-necessarily differentiable as piecewise linear functions, the set of non-differentiability points is equal to J^1.

Finally, the proposed denoising method is in charge of identifying the sets J^0 and J^1, in addition to provide denoised estimates of the experimental resonance frequency traces in space $\mathcal{D}^1$.

Remark 1. *Under the experimental conditions, some trace portions between two discontinuities may contain only two points. These trace portions should not be considered as "true" drifts according to the previous definition. Indeed, we cannot expect to extract interesting information from them because the proposed modeling space exactly fits every linear polynomial whose duration is two points. Hopefully, this situation rarely occurs. Because the particle deposition rate on the NEMS is much lower than the frequency sampling rate, the end point of a discontinuity and the beginning point of the next discontinuity are generally separated by more than two points. Even if such a situation occurs, the proposed denoising method is unaffected.*

Remark 2. *The frequency traces in the present report are functions of $\mathcal{D}^1$ and the frequency traces in [10] are elements of $\mathcal{D}^0$. However, the definition of both spaces shows that $\mathcal{D}^0 \subset \mathcal{D}^1$. Thus, the mathematical model presented here can also be understood as a generalization of the model presented in [10].*

Remark 3. *In our model, we imposed that J^1 is identical for both resonance frequency traces. Such a choice is made for numerical purposes and does not rely on physical considerations. Nevertheless, this constraint is not restrictive, because according to the above definitions, functions in $\mathcal{D}^1$ are differentiable everywhere except maybe on some points of J^1. Thus, if point p is truly a non-differentiable point for the first resonance frequency but not for the second, p is still an element of J^1. Consequently, J^1 is not a minimal set.*

B. TRACE FEATURES DETECTION

Locating discontinuities in resonance frequency traces is a problem which was already addressed through a specific method, the so called "ellipse method" [6]. In short, this method first forms N two-dimensional vectors $\mathbf{v}^i = ((\nabla \mathbf{f}^1)_i, (\nabla \mathbf{f}^2)_i)^T \ i = 1, \ldots, N$, and then compares each vector $\mathbf{v}^i$ to the level of noise affecting both frequencies. If vector $\mathbf{v}^i$ is above the noise level (up to the user's choice), then a discontinuity is identified at point i, otherwise no discontinuity occurs at i. The complete description is provided in Appendix A.

This method is very intuitive because it is strongly inspired by NEMS physics. Moreover, it provides satisfactory results for resonance frequency traces when drifts are absent [10]. Although it might be interesting to reuse it in the present context, this method does not rely on a precise mathematical framework. This induces a potential lack of reliability when analyzing experimental measurements containing drifts.

Thus, we proposed to interpret this "ellipse method" as a χ^2_2 statistical test where the statistical significance level is a simple function of the noise level, as defined by the "ellipse method". For proofs, the interested reader can refer to Appendix A. Besides all the mathematical tools that this interpretation gives access to, we can now point out the main defect of the "ellipse method". As χ^2_2 statistical test, the "ellipse method" is based on a statistic, which is the sum of two squared independent Gaussian variables, with 0 means. With drifts in resonance frequency traces, the "ellipse method" can no longer be reduced to such a test, but can be viewed as a non-central χ'^2_2 test with a noncentrality parameter that depends on drift slopes. However, using the methodology described in this report, the drift slopes are not known beforehand. They are estimated after the denoising steps, which require the discontinuity locations set J^0 as an input parameter. In conclusion, the "ellipse method" is rigorously inadequate for identifying discontinuities into traces with drifts and cannot be adapted easily to this type of data. Nevertheless, this defect can be partially overcome by using a simple hypothesis. Indeed, the "ellipse method" identifies trace discontinuities

as signal events that have intensities much higher than the usual gradients of resonance frequency traces. However, in portions of the traces corresponding to drifts, the aforementioned gradients are mainly equal to the local slopes of the drifts. We deduced that to keep acceptable false detection rate with the "ellipse method", trace discontinuities must be much higher than the local slopes of the drifts. Although this appears particularly constraining, most of our experimental measurements support the hypothesis of small drift slopes. Therefore, we assumed that this is generally true throughout the rest of this report.

Let us now tackle the problem of drift "detection". Once the trace discontinuity locations are identified, all drift locations are known by definition. However, drifts are also modeled as continuous piecewise linear functions, that is, as a set of several consecutive linear polynomials. Since a linear polynomial is perfectly defined with only two points, we must identify, for every drift, all points that could represent the boundary between different yet consecutive linear polynomials. This is equivalent to searching for the set of non-differentiability points J^1. In the absence of noise and for traces modeled as functions in $\mathcal{D}^1$, a point $p \in J^1$ is easily identified. Indeed, p belongs to J^1 if and only if the right derivative at p (i.e., the right local slope at p) is different from the left derivative at p (i.e., the left slope at p). This criterion must be revisited in the presence of noise because, for a function in $\mathcal{D}^1$ and a point $p \notin J^1$, it may modify the values of the points preceding and following p such that the left and right derivatives are no longer equal. However, when the noise level is low, it only slightly modifies the derivative values. Although different, they should remain close to each other. Consequently, the criterion chosen for the non-noisy case must be slightly changed by imposing a tolerance on the variation of the right and left local slopes at point p.

Since our goal is to propose a novel denoising method to enhance the mass resolution of our NEMS-spectrometer, we addressed the problem of identifying the elements of set J^1 using a specialized change detection library, called "ruptures" [14]. This PYTHON library provides a framework that is well-adapted to our needs. For a single trace, it determines the elements of J^1 in such a manner that the traces built on this set, as continuous piecewise linear functions, minimize a certain L^2 cost function. However, because we want the first two resonance frequencies to belong to the same function space $\mathcal{D}^1$, the provided tools must be adapted to obtain the same set J^1 for both frequencies. This can be done in many different ways, the simplest one being to compute a set of non-differentiability points for each resonance frequency trace and then merge them into a single set.

Remark 4. *In the library "ruptures", determining a set of non-differentiability points without prior knowledge of its size depends on a threshold: The higher the threshold, the fewer points J^1 contains. Consequently, the size of J^1 seems to rely entirely on the user's choice, and thus seems to be subjective and/or case-dependent. In fact, we will show that our denoising model avoids this pitfall by providing a tool that automatically selects the correct threshold to obtain the best model according to a given criterion.*

VI. DENOISING MODELING

In this section, we present the mathematical model used to denoise the resonance frequency traces from true NEMS experiments. While demonstrating the main ideas that underlay Problem (2) remain valid in an experimental context, we illustrate how to incorporate the introduced modeling features to obtain a meaningful representation of drifts. We then prove that the proposed model can be solved with a specific numerical algorithm, the latter accounting for the main NEMS physical features. Finally, we demonstrate that this algorithm converges towards a local minimum, proving that the corresponding estimates of both resonance frequency traces are locally optimal.

A. PRELIMINARIES

Before entering into detail, we recall another equivalent formulation of (2), which was implicitly introduced in [10]:

$$\left(\hat{\mathbf{u}}^1, \hat{\mathbf{u}}^2\right) := \underset{\substack{\left(\mathbf{u}^1,\mathbf{u}^2\right)\in\mathbb{G}^0\times\mathbb{G}^0 \\ \mathbf{u}^2=\mathbf{\Phi}\mathbf{u}^1,\mathbf{\Phi}\in\mathbb{H}}}{\arg\min} H_1\left(\mathbf{u}^1\right) + H_2\left(\mathbf{u}^2\right) \tag{3}$$

Where the functionals H_i $i = 1, 2$ is defined as:

$$H_i\left(\mathbf{u}^i\right) := ||\mathbf{M}\mathbf{u}^i||_1 + \frac{\lambda_i}{2}||\mathbf{W}^i\mathbf{u}^i - \tilde{\mathbf{f}}^i||_2^2$$

And where we have set for:

$$\mathbf{u}^i := \mathbf{G}\mathbf{v}^i$$
$$\mathbf{W}^i := \mathbf{V}^i\mathbf{G}$$
$$\tilde{\mathbf{f}}^i := \mathbf{V}^i\mathbf{f}^i$$

Problem (3) requires comments before proceeding further. Observe that Problem (3) is derived from (2), owing to the replacement of $\mathbf{v}^i$ for $i = 1, 2$ by their equivalent gradient-like vectors $\mathbf{u}^i := \mathbf{G}\mathbf{v}^i$. This change of variables is important because it increases the capability of our modeling to obtain realistic estimates of resonance frequency traces and comes in addition to the other modeling elements of Problem (2). Owing to this manipulation, the coupling between trace discontinuities is not handled through a constraint, but is explicitly incorporated in the functional to minimize. In doing so, the numerical scheme presented in this report exhibits interesting mathematical properties while maintaining a low computational cost.

When drifts are present in resonance frequency traces, controlling the gradient of the traces is a fundamental question that is applicable not only to discontinuities but also to drifts through the L^1 norm. Contrary to the situation in [10], the L^1 norm of the modeled traces is not zero for drifts. In fact, up to the sign, they are equal to the sum of the slopes of the linear

polynomials that constitute them. Thus, using the L^1 norm on drifts also minimizes these drift slopes over the entire trace length. Does this idea make sense ? We believed that this is desirable. Because we chose to use a minimization problem as a denoising process, we are in fact looking for a minimal explanation that could represent the recorded signals. In that sense, trying to minimize the total drift slope seems natural, because in ideal cases, they should be equal to zero. Nevertheless, using L^1 norm for drifts implies that the algorithms proposed in [10] can no longer be applied. We concluded that some changes in these algorithms are required. The following sections clarify these changes and provide adapted numerical schemes to solve (3). However, if such changes are necessary to consider drifts, they do not imply a total philosophy shift in the resolution of Problem (3), and we show that a three-step algorithm is always mandatory to obtain acceptable trace estimates.

B. STEP 1: VALIDATION OF TRACE FEATURES MODELING

To obtain estimates of experimental resonance frequency traces with drifts, we propose an approach involving the solution of two simpler minimization problems:

$$\hat{\mathbf{u}}^i := \underset{\mathbf{u}^i \in \mathbb{G}^1}{\arg\min}\, P(\mathbf{u}^i) \quad \text{for } i = 1, 2 \tag{4}$$

where the function P is defined as:

$$P(\mathbf{u}^i) := ||\mathbf{W}^i \mathbf{u}^i - \tilde{\mathbf{f}}^i||_2^2$$

Contrary to the function spaces modeling different structures of traces, we first notice that matrices $\mathbf{W}^i$ for $i = 1, 2$ are identical in Problems (3) and (4). Because these matrices are designed to only consider noise features and because noise features are totally independent of trace modeling, there is no reason to search for new formulations. Naturally, the previous argument extends to the following denoising steps. Thus, we can observe that Problems (4) are simple quadratic problems under constraints. These types of problems are well-known, and many numerical methods exist for solving them efficiently. Among these methods, we chose the FISTA algorithm [15]- [16], which is a special case of accelerated gradient descent algorithms [17]- [20]. The FISTA algorithm ensures fast convergence while being simple to use, but requires an auxiliary mathematical operator to work. In the present case, this operator is a projector onto space $\mathbb{G}^1$ the expression of which is given in Appendix B.

Despite their simplicity, Problems (4) provide interesting information. Indeed, they can also be considered as a way to measure the relevance of our trace feature modeling. To illustrate this point, let us consider a single set of trace discontinuities, denoted as J^1, but with two different models of trace space, denoted as $\mathcal{D}_1^1$ and $\mathcal{D}_2^1$ (or equivalently, two different vector spaces $\mathbb{D}_1^1$ and $\mathbb{D}_2^1$). We will assume in the following that drifts in $\mathcal{D}_1^1$ are modeled with fewer linear polynomials than in $\mathcal{D}_2^1$, i.e. $\mathcal{D}_1^1 \subset \mathcal{D}_2^1$. Finally, we denote $\mathbf{v}^{i,1}$ and $\mathbf{v}^{i,2}$ as the solutions of (4) for the i^{th} resonance frequency when drifts belong to $\mathbb{D}_1^1$ and $\mathbb{D}_2^1$ respectively. Based on the definition of (4) and the previous hypotheses, we can then write:

$$||\mathbf{W}^i(\mathbf{v}^{i,2} - \tilde{\mathbf{f}}^i)||_2^2 \leq ||\mathbf{W}^i(\mathbf{v}^{i,1} - \mathbf{f}^i)||_2^2$$

Hence, increasing the number of degrees of freedom in our mathematical modeling of drifts results in a reduction in the discrepancy between the estimated trace and experimental data. However, it should be noted that the previous errors can also be viewed as an estimation of the variance of the noise that affects the NEMS resonance frequency traces. Thus, they can be compared with the true noise variance. Consequently, if the true noise variance is lower than the estimated noise variance coming from a given drift model, the latter is too coarse and could be refined to obtain higher variance estimates. On the other hand, if the true noise variance is higher than the estimated noise variance coming from a given drift model, the latter is too fine and could be coarsened to obtain lower variance estimates. Problems (4) can then be used to obtain acceptable estimates of the true resonance frequency traces, but without controlling the trace discontinuity amplitude, and consequently the particle mass resolution. In short, solving the Problems (4) can only be regarded as a preliminary step in the entire denoising process.

Remark 5. *Note that the same reasoning applies to selecting a model that estimates the correct number of trace discontinuities in experimental signals. Thus, Problems (4) also ensure the selection of the correct discontinuity model.*

C. STEP 2: COMPUTING DENOISING PARAMETERS

In this step, the main objective is to solve intermediate minimization problems, whose solutions enable the computation of the numerical parameters necessary for the last denoising step. To enhance the similarity between the present minimization problems and the final nonlinear problem, these problems adopt a form in which the discontinuities of the resonance frequency traces are controlled through L^1 terms:

$$\hat{\mathbf{u}}^i := \underset{\mathbf{u}^i \in \mathbb{G}^1}{\arg\min}\, T(\mathbf{u}^i) \quad \text{for } i = 1, 2 \tag{5}$$

where the functional T is defined as:

$$T(\mathbf{u}^i) := ||\mathbf{L}\mathbf{u}^i||_1 + \frac{\lambda_i}{2}||\mathbf{W}^i \mathbf{u}^i - \tilde{\mathbf{f}}^i||_2^2$$

In Problems (5), the penalization parameters λ_i ($i = 1, 2$) are originally unknown. Intuitively, they must be set such that the L^2 terms (which can be considered as noise variance estimates) are sufficiently close to the experimental noise variances. Thus, providing a method to compute the correct λ_i is a fundamental question. Fortunately, this question was addressed in various general contexts in different articles, such as [21] and [22], and extended to resonance frequency traces from simulated data in [10]. The main idea is to iteratively solve the targeted penalized minimization problem while updating the penalization parameter until the estimated variance closely matches the experimental variance. The

update of penalization parameters can be carried out automatically until convergence, as described in [21] and [22], thereby eliminating the need for both predetermined values and human intervention.

However, contrary to [10] where the penalized problem is quadratic, Problems (5) are only strictly convex, which hinders the use of the exact same algorithm for estimating λ_i. In fact, Problems (5) are similar to the convex penalization problems studied in [22]. The difference lies in the solution space $\mathbb{G}^1$, which includes modeling constraints, in contrast to [22], where no constraints are imposed. Consequently, it seems natural to adapt the method presented in [22] to our specific context. This implies that an adapted proximal method is necessary to estimate the λ_i parameters, similarly to what is presented in [15], [16], [23]. In our case, because discontinuities and drifts belong to disjointed sets, the definitions of well-suited proximal operators are explicit (see Appendix B), and thus enable fast solving using the FISTA algorithm.

Remark 6. *Let denote $\mathbf{v}^i$ and $\mathbf{w}^i$ for $i = 1, 2$ as the solutions to Problems (4) and (5), respectively. Then, for all $\lambda_i > 0$, we necessarily have:*

$$||\mathbf{W}^i\mathbf{v}^i - \tilde{\mathbf{f}}^i||_2^2 \leq ||\mathbf{W}^i\mathbf{w}^i - \tilde{\mathbf{f}}^i||_2^2$$

This inequality shows that if the estimated noise variances obtained by solving (4) are above the experimental noise variances, then Problems (5) cannot provide noise estimates with lower variances. It then seems unnecessary to resolve Problems (5) in addition to Problems (4). Nevertheless, we recall that Problems (4) do not control the amplitude of discontinuities, unlike Problems (5), and thus do not provide control over particle mass resolution, which is yet to be achieved. To solve this issue, it is necessary to select a trace feature model such that Problems (4) provide the estimated noise variances below the experimental noise variances. In doing so, we have a chance to determine parameters λ_i such that Problems (5) provide accurate noise approximations while also preserving mass resolution.

D. STEP 3: NONLINEAR DENOISING

Now, we solve a problem similar to (3), but incorporate all the previously introduced concepts. In practical terms, we propose the following model:

$$\left(\hat{\mathbf{u}}^1, \hat{\mathbf{u}}^2\right) := \underset{\substack{\left(\mathbf{u}^1,\mathbf{u}^2\right)\in\mathbb{G}^1\times\mathbb{G}^1 \\ \mathbf{u}^2=\mathbf{\Phi}\mathbf{u}^1,\ \mathbf{\Phi}\in\mathbb{H}}}{\arg\min} U_1\left(\mathbf{u}^1\right) + U_2\left(\mathbf{u}^2\right) \quad (6)$$

Where the functional U_i $i = 1, 2$ is defined as:

$$U_i\left(\mathbf{u}^i\right) := ||\mathbf{L}\mathbf{u}^i||_1 + \frac{\lambda_i}{2}||\mathbf{W}^i\mathbf{u}^i - \tilde{\mathbf{f}}^i||_2^2$$

In (6), the parameters λ_i for $i = 1, 2$ are the ones determined in the previous denoising step.

This problem is not as simple as the previous ones because it is constrained; unknowns $\mathbf{u}^1$ and $\mathbf{u}^2$ are coupled through the matrix $\mathbf{\Phi}$ as stated in System (1). Nevertheless, it represents a natural generalization of Problems (5), as it reduces to the two corresponding equations in the absence of constraint on $\mathbf{u}^1$ and $\mathbf{u}^2$. A natural way to consider the coupling between $\mathbf{u}^1$ and $\mathbf{u}^2$ is to use a Lagrangian multiplier, but this has a drawback: It introduces an additional variable that must be computed as well. The resulting algorithm would be expensive in terms of computational cost and would thus not be suitable for large data. We developed another approach, detailed in Appendix C. The matrix $\mathbf{\Phi}$ is explicitly introduced in U_i, for $i = 1, 2$, by substituting the discontinuities in the second resonance frequency trace with a suitable transformation of the discontinuities in the first resonance frequency trace. In short, we proceeded to a change of variable that generates a new "uncoupled" functional equivalent to the functional in (6) but which depends on the three variables $\mathbf{u}^1$, $\mathbf{D}\mathbf{u}^2$ and $\mathbf{\Phi}$. In a more explicit manner, each variable $\mathbf{u}^i$, for $i = 1, 2$, is expressed as the sum of two vectors $\mathbf{D}\mathbf{u}^i$ and $\mathbf{J}\mathbf{u}^i$. Subsequently, we substituted these expressions for $\mathbf{u}^i$ into $U_i\left(\mathbf{u}^i\right)$. Finally, we implemented the constraint in (6) by replacing $\mathbf{J}\mathbf{u}^2$ with $\Phi\mathbf{J}\mathbf{u}^1$ in the functional U_2. As a result, the constraint between $\mathbf{u}^2$ and $\mathbf{u}^1$ is explicitly incorporated into the functional to be minimized. The only remaining constraint in (6) is that $\mathbf{\Phi} \in \mathbb{H}$, but it is easily handled owing to its simple structure. Technical manipulations and additional details regarding space $\mathbb{H}$ can be found in Appendix C.

However, the resulting minimization problem has no mathematical properties to obtain unique estimates for both resonance frequency traces [24]. Despite this drawback, we developed an algorithm that computes estimates of the resonance frequency traces, and we claim that these estimates are optimal according to some criteria. Without entering the technical details, which are accessible in Appendix C, the corresponding algorithm can be written as follows:

Algorithm 1 Compute $\hat{\mathbf{u}}^1$, $\hat{\mathbf{u}}^2$ and $\mathbf{\Phi}$ as solutions of Equation (6)

$j \leftarrow 0$
repeat
  $j \leftarrow j + 1$
  $\mathbf{v}^{1,j}, (\mathbf{D}\mathbf{v}^2)^j \leftarrow \underset{(\mathbf{u}^1,\mathbf{D}\mathbf{u}^2)\in\mathbb{G}^1\times\mathbf{D}\mathbb{G}^1}{\arg\min} F(\mathbf{u}^1, \mathbf{D}\mathbf{u}^2, \mathbf{\Phi}^{j-1})$
  $\mathbf{\Phi}^j \leftarrow \underset{\mathbf{\Psi}\in\mathbb{H}}{\arg\min} F(\mathbf{u}^{1,j}, (\mathbf{D}\mathbf{u}^2)^j, \mathbf{\Psi})$
until user's threshold is reached
$\hat{\mathbf{u}}^1 \leftarrow \mathbf{v}^{1,j}$
$\hat{\mathbf{u}}^2 \leftarrow \mathbf{J}\mathbf{\Phi}^j\mathbf{v}^{1,j} + (\mathbf{D}\mathbf{v}^2)^j$
$\mathbf{\Phi} \leftarrow \mathbf{\Phi}^j$

We observe that this algorithm iterates on two subproblems, each of them having a specific role. The first subproblem computes trace estimates with a fixed $\mathbf{\Phi}$, whereas the second computes matrix $\mathbf{\Phi}$ when trace estimates are fixed. Thus, the proposed algorithm is an alternating direction algorithm between the two subproblems, which do not have the same mathematical properties. Indeed, the first subproblem is a strictly convex problem under convex constraints, whereas

the second subproblem is a quadratic problem under constraints, this quadratic nature owing to prior knowledge of the signs of the trace discontinuities. Clearly, different techniques are necessary to solve each subproblem. The second subproblem is evidently the easiest to solve, and every standard algorithm that deals with constrained quadratic problems is acceptable. Because our constraint space is identical to that in (4), we chose the FISTA algorithm and the projection operator defined in (8) to solve it. For the first subproblem, we used a proximal method to handle the convexity property. In addition, the proposed algorithm does not impose any predefined relationship between the drifts in the first and second resonance frequency traces. This is a fundamental requirement because there is no indication that drifts in both traces are physically correlated. Thus, if a correlation exists, our algorithm will naturally reveal it. The only remaining difficulty is defining proper proximal and projection operators. With the definitions given above, these operators have explicit expressions that limit the computational costs. The expressions and corresponding proofs are detailed in Appendix B.

Remark 7. *Because Algorithm* 1 *does not possess a unique global minimizer, the question of initialization becomes crucial. Because Problem (6) generalizes Problems (5) by introducing the coupling of trace discontinuities, it seems natural to initialize Algorithm* 1 *with the solutions of (5). We applied this approach to the calculations.*

Remark 8. *The variable* $\mathbf{\Phi}$ *has another advantage: It allows for denoising of resonance frequencies without explicitly calculating the deposited particle positions. However, these positions are essential for calculating the mass of deposited particles, as shown in System (1). Therefore, a means of estimating these parameters retrospectively is required. Because we modeled* $\mathbf{\Phi}$ *as an element of* $\mathbb{H}$*, the constraint* $\mathbf{u}^2 = \mathbf{\Phi}\mathbf{u}^1$ *in Equation (6) and the second equation in System (1) leads to the following equality:*

$$\mathbf{\Phi}_{jj} = \frac{\mathbf{s}_j^2}{\mathbf{s}_j^1}\Phi(x_j)$$

where the j is the index of the j^{th} *deposited particle,* $\mathbf{s}_j^i$ *is the* i^{th} *resonance frequency, and* x_j *is the deposition position of the* j^{th} *deposited particle.*

It remains to compute every position x_j *by solving the above nonlinear equality, which can be done using adapted algorithms such as the those presented in [25] or [26]. Once every position is computed, the particle masses are estimated by solving the first equation in System (1). See Appendix C for further details.*

VII. EXPERIMENTAL VALIDATION

In this section, we present the results of our denoising process when applied to mass measurements of gold nanoparticles (AuNPs) and of capsid like particles (CLPs).

A. GOLD NANOPARTICLES

Gold particles were produced by BBI Solutions, and their shape is assumed to be spherical with a diameter of 29.2 ± 2 nm (BBI product code : EM. GC30). With these dimensions, a particle has a mass of $25.16\ 10^{-20}$ kg or equivalently 151.51 megadalton (MDa). The measurement data were acquired using the experimental system schematically described in Figure 2. The latter is composed of a microfluidic system that transports the particles in methanol (concentration of approximatively 10^{11} particles$/$mL) at a flow rate of 30μL/h, a nebulization system that aerosolizes the solvated particles at ambient pressure (using Electrospray Ionization under 2.18 kV), a heated capillary that removes the solvent coating of the aerosolized particles (at 200°C), and an aerodynamic lens that focuses the aerosolized particles towards a NEMS array located in a chamber at $1.3\ 10^{-2}$ mBar. The NEMS array is composed of 20 NEMS in silicon whose actual dimensions -and thus masses- are known ($L \times 300$ nm $\times 160$ nm, with L gradually varying from 7 μm to 9.2 μm). These data were acquired during two experiments under constant environmental conditions (room temperature 25°C, relative humidity 25%). In both the experiments, the NEMS array was identical. This indicates that the particles that landed on the NEMS during the first experiment still adhered to the device during the second experiment. Owing to technical constraints, the data of each experiment were recorded in two consecutive files. This splitting has no consequences on the final results because it does not affect the NEMS physics. The total duration of each experiment was 4200s equally divided between the two recording files. Each NEMS resonance frequency was sampled every 0.4s.

To obtain the particle mass distribution, two different methods were used. The first, denoted as WDM hereafter, consists of computing the particle mass without prior denoising of resonance frequency traces. This method was employed in several reports for data treatments (see [1], [2], [13]) and was consequently used as a reference method. Despite its simplicity, WDM is a pertinent method to obtain a particle mass distribution in the presence of noise only. With no noise filter and providing a large number of detected particles, the mean of the computed mass distribution should follow the Law of Large Number (LLN) and thus should converge towards a statistically reliable estimate of particle mass. The variance in the distribution of particle masses serves as an indicator of mass resolution, because it represents a measure of dispersion around the mean of the particle mass distribution. However, with drifts, WDM may not be as pertinent because perturbations in NEMS signals cannot be modeled as pure statistical events. Consequently, we expect the mean of the particle mass distribution to be less accurate and the variance to be impacted. The second method was based on the TV algorithm presented in the previous section. Removing the noise from frequency traces (as described in Steps 1 to 3 in the denoising modeling section) and computing the mass distribution from

the resulting profiles (as described in Remark 8) affect both the mass accuracy and mass resolution. If we expect the former to not change significantly, we anticipate a gain in mass resolution when compared with the WDM estimate. We note that the number of detected particles is almost similar for the two experiments: 3015 for the first experiment and 2670 for the second (a variation of 11.5%). Thus, both experiments play similar roles when considering the overall number of deposited particles (the first experiment represents 53% of the deposited particles and the second experiment 47%).

For both resonance frequencies, we automatically estimated noise features (such as the Power Spectral Density of each trace and the noise covariance matrix) at the beginning of each experiment, when no particle deposition occurred. These noise features were then used to design matrices $\mathbf{V}_i$ for $i = 1, 2$, following the methodology described in [10], and to set the "ellipse" method parameters for subsequent particles detection (with a Type I error below 1%, see Appendix A). Of course, these "ellipse" method parameters were set to the same values for both WDM and TV methods. This implies that the J^0 set is identical in both cases; thus, the detected particles are the same. To identify the set of non-differentiability points $\mathbb{P}$, we used the "rupture" package described in [14]. In this library, we selected the "CLinear" model to represent a frequency trace as a continuous piecewise linear function, and the PELT algorithm to detect every element of $\mathbb{P}$. This algorithm efficiently detects variations in the local slope of a trace, while maintaining a linear computational cost. Nevertheless, it also requires a penalization parameter μ: The higher the value of μ, the fewer linear polynomials are necessary to define a single drift. Consequently, we defined a fixed set of acceptable values for μ (here $\{10^4, 10^5, 10^6, 10^7, 10^8, 10^9\}$), and always selected the highest value in this set that satisfies Remark 6. The parameters λ_i for $i = 1, 2$ in Problems (5) were calculated using the method described in [22], with two stopping criteria: A relative error in the noise variance equal to 1% and a relative error in successive λ_i values equal to 10^{-5}.

1) Influence of drift modeling

First, we demonstrate how our drift modeling affects trace representation. In Figure 3, we show a section of the first resonance frequency trace before denoising and after applying our TV-based denoising method. This figure clearly shows that our model produces denoised traces that are piecewise linear, which seem to be coherent with the experimental (noisy) signal.

Figure 4 displays the same trace portion, denoised with identical parameters, except for those related to the PELT algorithm. We deliberately selected a parameter μ, which is smaller than in the previous example, to obtain a set $\mathbb{P}$ with more elements. With such a choice, we obtain a resonance frequency trace exhibiting more complex variations at smaller time scales while still closely following the noisy experimental trace. A graphical comparison is shown in Figure 4.

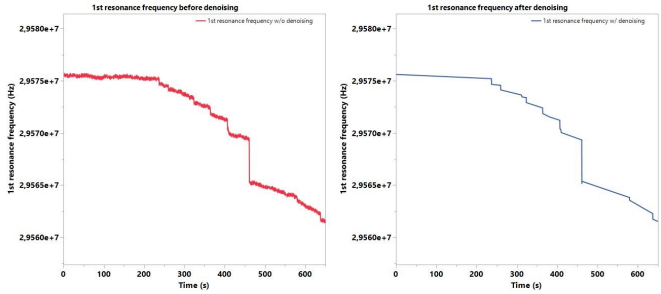

FIGURE 3. **Left: First resonance frequency trace before denoising between 0s and 650s. Right: First resonance frequency after denoising between 0s and 650s. Observe that portions of the denoised trace are clearly represented by piecewise linear functions.**

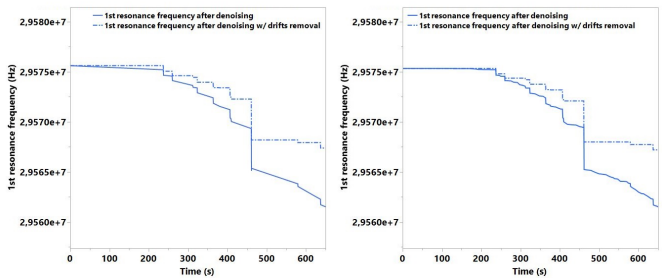

FIGURE 4. **First resonance frequency trace when denoised with two values of PELT parameters μ and when drifts are removed after post-treatments. Left: First resonance frequency denoised with $\mu = 10^9$ (solid blue) and after drifts removal (dashed blue). Right: First resonance frequency denoised with $\mu = 10^4$ (solid blue) and after drifts removal (dashed blue). We observed the expected result: A lower value of μ better captures small time scale variations in the resonance frequency trace. The dashed blue functions represent the trace we would have obtained in the absence of drifts, corresponding to the theoretical shape of the resonance frequency.**

In addition to showing the consistency of our drift modeling, the previous graphical examples also illustrate the versatility of our TV-based denoising method. With an appropriate change in parameter, we are indeed able to compute consistent denoised resonance frequency traces that can capture variations at different time scales.

2) Particle mass computation

Let us focus on computing the mass computation of gold nanoparticles when either the WDM or TV-based methods are used to treat the resonance frequency traces. To achieve statistical significance, we applied the same process to both numerical methods: We computed the mass of every detected particles in every NEMS for every experiment, and gathered the results into a single dataset. This yields a larger number of detected particles than when considering every NEMS separately. It should be noted that for both methods, the number of detected particles is identical before any denoising or filtering process. This implies that only the mass distribution varies. Among the masses obtained, we applied a filter to eliminate inconsistent results. As explained in [10], this process

is mandatory and does not depend on the chosen method. Indeed, even for simulated data where all parameters are perfectly known, such inconsistencies exist and are unavoidable. They are the consequences of the mathematical properties of System (1), which shows intrinsic instabilities outside the useful range of $[0.27, 0.48] \cup [0.52, 0.73]$ (for a normalized NEMS length). Thus, we removed from the resulting mass distribution all particles whose computed positions do not belong to $[0.27, 0.48] \cup [0.52, 0.73]$.

We now summarize the results obtained for a mass interval of $[50, 250]$ MDa in Table 1 and Figure 5. We selected this mass interval with its center aligned to the anticipated mass of gold nanoparticles with a diameter of 29.2 nanometers. The chosen bounds are sufficiently distant from the center to reveal the characteristics of the mass distribution tails.

	BBI gold nanoparticles	TV based	WDM
mass mean (MDa)	151.51	151.82	162.66
mass variance (MDa)	N/A	27.63	32.92

TABLE 1. Table of mass distribution statistics for TV-based and WDM methods in the mass interval [50, 250] MDa, with BBI AuNPs as a reference. In this interval, the total number of detected particles was 311 and 308.

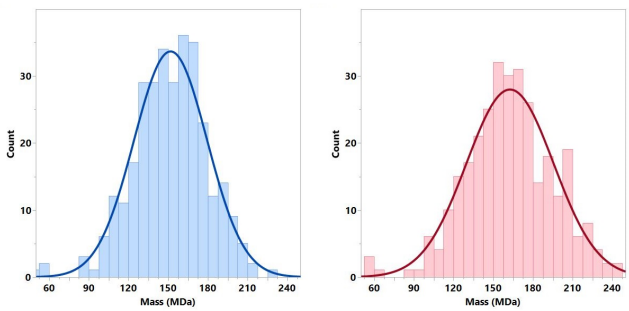

FIGURE 5. AuNP mass distribution profile for TV-based denoising and WDM methods in the mass interval [50, 250] MDa. Bin size is equal to 7.5 MDa. In this interval, the total number of detected particles is respectively equal to 311 and 308. Left: Mass distribution profile for the TV-based denoising method. Right: Mass distribution profile for the WDM method.

We first observe that the mean mass obtained by the TV-based method is close to that obtained using the manufacturer's values. We also note that the relative error value (0.7%) is in line with the results presented in [10], where no drifts are present. This confirms that drifts are well captured by our model. In constrat, the WDM method gives a mass estimate that overestimates the true particle mass, while having a mean mass relative error (around 7%) one order of magnitude higher than that shown in [10]. For the WDM method, such an increase in the mean mass relative error between the present study and the aforementioned one suggests that drifts are important signal features to consider when attempting to obtain consistent mass estimates. In addition to the impact of drifts on the mean mass estimate, the previous results also suggest that drifts do not share the same physical origin as white or colored noise, that is, they cannot be modeled as random effects; in that case, WDM mean mass should follow the LLN and be closer to the mean mass estimated with the manufacturer's value. Finally, we note that the proposed TV-based method is more accurate than the WDM method by a factor of ten. This increase in accuracy is particularly significant in the field of mass spectrometry. Indeed, mass spectrometry characterizes the different components of a sample through their mass [27]. Thus, the more accurate the mass measurement, the more reliable the component identification. Therefore, it is important to develop a method that ensures a high level of accuracy.

Remark 9. *We observe that the mean mass obtained using the TV-based method is lower than the mean mass obtained using the WDM method. This tendency should always be verified. Indeed, the TV-based method minimizes the sum of trace gradients, which implies that it also minimizes the sum of all particle masses. Consequently, we deduce that the sum of all particle masses for the WDM method is greater than that for the TV-based method. Naturally, this is the same for the respective means.*

The proposed TV-based denoising method behaves differently according to the experiment. For each NEMS, the number of linear polynomials used to model the drifts is much higher during the second experiment than that during the first experiment (see Table 2).

	1st experiment	2nd experiment
Number of linear polynomials	46496	75272

TABLE 2. Table of the number of linear polynomials for drift representation for all NEMS and a single resonance frequency

This difference in the resonance frequency trace representation may be a sign of the physical differences in the NEMS between the first and the second experiments. According to the protocol described above, the NEMS were cleaned of particles for the first mass measurement experiment and reused for the second experiment. In fact, the surface state of the NEMS in the second experiment was therefore different from that in the first one. Nevertheless, this change in drift representation does not strongly change the mass distribution profile. In our modeling, drifts are indeed identified after trace discontinuities caused by particle deposition. Because these discontinuities are unaffected by the level of drift modeling, the computed particle masses should be mostly similar to the previous case. This assertion was verified by conducting new mass computations, which are described and analyzed in Appendix C.

For these experiments, in addition to a gain in mass accuracy, we observe a non-negligible gain in mass resolution (approximately 16.07%) for the TV-based method compared with the WDM method. Such a gain could be very interesting for experiments in which two types of particles with similar masses are studied. We can expect a better discrimination be-

tween these two types of particles with the TV-based method, whereas it could be more difficult with the WDM method. We also observe that the gain in resolution shown here is not as good as that shown in [10]. In the aforementioned report, the mass resolution is estimated using simulated data, where every particle mass distribution is exactly the Dirac function before the addition of noise. Thus, the observed loss in the mass resolution is only due to noise effects. In the present case, the situation is different because the particle mass distribution deviates from a Dirac function owing to the fabrication processes. The particles have a natural mass spread, which creates a mass distribution with a non-negligible support that limits the mass resolution. As the TV-based denoising method removes noise, it focuses on limiting the loss of mass resolution owing to noise, but it has no effect on the natural spread of the particle mass. The observed gain in the mass accuracy is then bounded and cannot exceed a certain value.

3) Drift interpretation

In this section, we focus on comparing the experimental data with the modeling described in Appendix F. For ease of reading, we recall that our modeling assumes that the NEMS operate in an atmosphere composed of different gases: Air at low pressure and a gas generated by the evaporation of the liquid solvent. This mixture of gases is assumed to be uniformly adsorbed by the NEMS, both in time and space, thus increasing their total mass. This hypothesis is related to observations made in the field of gas sensors, where sensor surfaces are deliberately functionalized to adsorb specific molecules [28]. As a by-product, this model predicts a regular and smooth decrease over time for both resonance frequencies, exhibiting a certain correlation factor. However, an analysis of our experimental resonance frequency traces does not show clear evidence of this temporal behavior. If the traces seem to exhibit time structures that could correspond to the expected ones, the number of data points is too low to make a definitive decision. A similar observation can be made when looking for a correlation between the decrease in both resonance frequency traces. No strong evidence emerges even if some positive trends appear (see Appendix F).

However, our experimental results may also indicate that some of our modeling hypotheses must be modified. It could be more realistic to consider random and spatially discontinuous droplet depositions. In such a scenario, NEMS surfaces would vary gradually over time from an initial smooth state to various rougher states. Consequently, a variable surface interaction between the NEMS and its surrounding environment would occur, explaining both the lack of time correlation between the resonance frequency drifts and the drifts' long-term behavior observed in our data.

Eventually, it appears that additional experimental data are required to validate or differentiate between the two previous models: Continuous homogeneous droplet deposition and random discontinuous droplet deposition. However, even if additional data invalidated the homogeneous deposition modeling, it would not automatically validate the inhomogeneous deposition case owing to the lack of existing modeling. In this situation, it would be interesting to directly image the NEMS surfaces at different times (using Scanning Electron Microscopy [29] or Atomic Force Microscopy [30] methods), and check their actual state and evolution over time. These images could confirm inhomogeneous modeling or provide some hints about the underlying physics that controls the drift behavior.

B. CAPSID LIKE PARTICLES

In this section, we measured the mass of transpoviron free Zamilon vitis virophage capsids [31], which are assimilated to CLPs. Virophages are true viruses of giant viruses belonging to the family *Mimiviridae* [32]. Virophage capsids (also known as virions) are the protein shells that encapsulate the genetic material of virophages. Zamilon virophage capsids have the same structure as Sputnik virophage capsids [33] whose icosahedral structure has been determined by cryo-electron microscopy [34]. The icosahedral capsid is organized into a $T = 27$ lattice with 260 trimeric capsomers, composed of three double "jelly-roll" major capsid proteins, the most abundant protein in the virions. Additionally, there are 12 pentameric capsomers made of five single jelly-roll proteins. Mass spectrometry-based proteomics identified additional proteins with variable abundance [31], the vast majority being inside the capsids, with some also decorating the surface of the icosahedral capsids. Finally, the virions contain the 20 kilo-base pair (Kbp) double-stranded DNA (dsDNA) genome. Despite this regular structure and their known protein composition, obtaining precise mass measurements of virophage capsids remains a challenge. For instance, the proteins at the periphery of the capsids can be partially lost during the purification procedure, altering the overall mass to different extents and impacting their diffusion capabilities. It has been demonstrated that NEMS are innovative and useful tools for measuring the mass of capsids [8], but it has also been found that a denoising process is necessary to increase the precision and resolution of mass measurements in order to differentiate capsids presenting various compositions.

The Zamilon vitis virophage was replicated by the giant virus Moumouvirus maliensis in co-infected *Acanthamoeba castellanii* cells. The virophage was then separated from the giant virus by centrifugation and several rounds of filtration, and finally purified on sucrose gradient. The pelleted virophage particles were resuspended in 40 millimolar (mM) Tris buffer, pH 7.5. The stock solutions were then diluted in deionized water to a concentration of about $5\ 10^{11}$ capsids per milliliter (i.e. by a factor of approximately 1000) for the mass analysis. The estimated mass of these CLPs is about 85 MDa to 90 MDa, contributed by both the virophage proteome and the dsDNA genome. Since there were 780 copies of the major capsid protein in the icosahedral capsids, the copy number of the other proteins was estimated based on their relative abundances in the mass spectrometry-based proteomic analysis of the virophage. The nucleotide sequence

of the virophage genome was also used to compute its mass. The capsid mass estimation was simply derived by summing the masses of the different proteins composing the virophage capsid and the mass of the genome. Similar to AuNPs, the mass measurement data were acquired with the system described in Figure 2, along with the same microfluidic and nebulization systems. The mass measurements represent 17 different experiments (numbered following chronological order), conducted over several months. Therefore, while the experimental conditions were similar across experiments, they were not exactly identical. The relative humidity fluctuated within a few percentage points around 25% and the room temperature similarly varied around 25°C. The microfluidic system transported the CLPs in solution to the nebulization system at a rate ranging from 30μL/h to 60μL/h, depending on the experiment. The capillary was heated at lower temperatures than for AuNPs, as biological samples are more sensitive to heat than nanoparticles. The chosen temperature range was from 150°C to 175°C. Finally, the Electrospray System was set from 2.6kV to 3.8kV depending on the experiment and pressure in the NEMS chamber was set at $1.3\ 10^{-2}$ mBar. A total of 5 different arrays of 20 resonators each were used for this 17 experiments. Since the architecture of these arrays and the NEMS features were identical, these replacements in NEMS arrays had no influence on the overall results. Also note that the NEMS in each array had dimensions identical to those indicated in the AuNPs section. Finally and similar to the AuNPs experiments, each NEMS resonance frequency was sampled every 0.4s during the whole duration of each experiment.

1) Mass computation

The measurements of all experiments were gathered to compute the mass distribution of CLPs, and then were treated with the WDM or the TV-based method. As the data are identical for both methods, the detected discontinuities due to capsid deposition are identical, and, thus, the overall number of detected particles is also identical. As for gold nanoparticles, we applied some position and mass filters to remove inconsistent results: Following the same arguments as in the AuNPs case, we remove particles whose computed positions do not belong to $[0.27, 0.48] \cup [0.52, 0.73]$ and whose computed masses is not in the range $[40, 150]$ MDa.

Before demonstrating what the impact of our TV-based method on the mass distribution profile is, we recall that for virophage capsids, there is no true mass reference that can be used as a comparison point. Contrary to gold nanoparticles, CLPs are not produced with a perfectly controlled industrial process. Therefore, the virophage capsid population we studied may have different compositions (due to the presence or loss of additional proteins) and the mean of the CLPs distribution mass only represents a mean of these capsid masses and not a unique type of capsid. Nevertheless, it is still pertinent to verify if the WDM and TV-based methods obtain comparable mass means and if these means are close to the estimated virophage capsid mass, which is computed by summing the masses of the structural proteins and genome that compose the capsid.

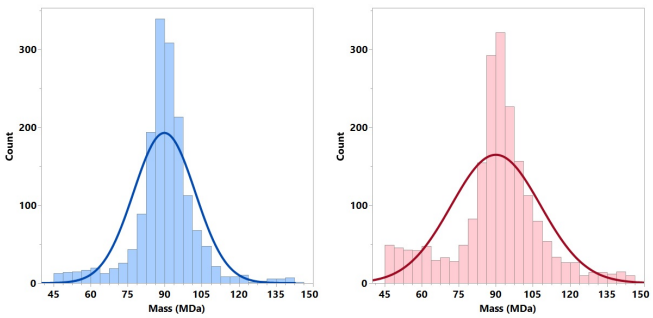

FIGURE 6. Capsid mass distribution profile for TV-based denoising and WDM methods in the mass interval [40, 150] MDa. Bin size is equal to 3.75 MDa. In this interval, the total number of detected particles is respectively equal to 1606 and 1988. Left: Mass distribution profile for the TV-based denoising method. Right: Mass distribution profile for the WDM method.

We first observe that the means of both mass distributions (89.87 MDa for the TV-based method and 90.03 MDa for the WDM) are close to each other and align with the estimated virophage capsid mass. This initial observation confirms the consistency of the TV-based method with the reference method. We also observe that, contrary to the gold nanoparticle experiments, the TV-based method has a similar mass precision to the WDM method when compared to the estimated capsid mass (5.5% relative error versus 6.8% for the 85 MDa estimate and 1% relative error versus 0.8% for the 90 MDa estimate). This can be explained by the difference in the number of detected mass events in both situations. Indeed, in this section, the number of detected masses in the targeted range is approximately 5 times higher than in the AuNPs experiments: Since the WDM method relies on statistical properties, it is favored by this situation. Conversely, this results seems to show that WDM needs a large number of mass events to achieve similar results to the TV-based method, and is therefore more time demanding. Additionally, we notice that the background signal in the TV-based method is lower than that obtained with the WDM, resulting in an increased signal-to-noise ratio. This difference can be attributed to the heavier left tail of the WDM mass distribution. It is noteworthy that this heavier tail for WDM is caused by the higher number of detected mass in the studied mass interval (approximately 20% higher). Since the total number of detected masses is equal for both WDM and TV-based method, this disparity can only be explained by the denoising process of the TV-based method, which produces resonance frequency discontinuities free from noise and drifts and, consequently, influencing the mass estimations.

Since we do not have true mass reference for virophage capsids, we consider another type of criterion to estimate the mass precision and resolution. When considering different

experiments, the variability of mass distribution across these experiments is a good indicator of the accuracy of an analysis method. Indeed, the more variability, the less accurate an experiment is. Nevertheless, using such a criterion necessitates experiments with the same experimental conditions to be reliable. In order to fulfill this requirement, we thus focus on 4 consecutive experiments among the 17 that were conducted the same day, and, thus, under the exact same experimental conditions. With this set of experiments, both TV-based and WDM method can be compared regarding the intrinsic variability of the mass distribution they contribute to produce. Additionally, we also compare the data spread of each experiments (i.e. the difference between the maximum mass and the minimum mass) in this set for each method: Since the mass distribution from the WDM method has a heavy tail that the TV-based method does not, using standard-deviation as a comparison criterion would excessively bias the results in favor of the TV-based method. Both criteria (distribution variability and data spread) are shown in Figure 7 and summarized in Table 3.

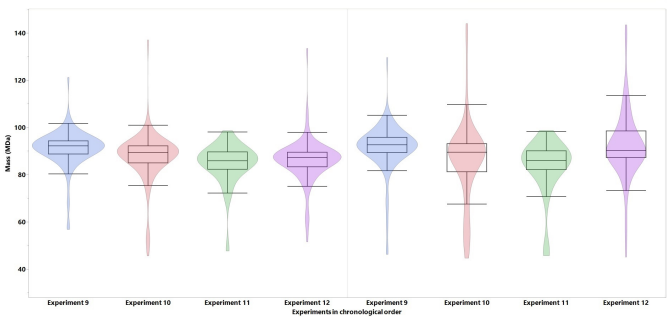

FIGURE 7. **Box plots and violon iso-response curves of capsid mass for TV-based denoising and WDM methods. Left: Box plots and violon iso-response curves for the TV-based denoising method. Right: Box plots and violon iso-response curves for the WDM method.**

	TV-based method			WDM		
	Nb of particles	median	spread	Nb of particles	median	spread
Experiment 9	111	92.1	63	116	92.5	81.5
Experiment 10	105	89.3	89.5	144	89.4	95.5
Experiment 11	35	85.8	50.27	37	85.96	51.73
Experiment 12	99	87.1	80.4	102	90.1	96.4

TABLE 3. **Main information about the mass distribution profile for the four experiments represented in Figure 7. The unit for the median and spread data is MDa.**

We observe that both methods yield similar results for each experiment in term of median values and exhibit a similar trend over time: A decrease for the first three experiments followed by an increase on the last day. When comparing the two methods, we also note that the variation in median values over time is of the same order of magnitude from one day to another. This indicates that the TV-based method provides mass estimations as reliable as the WDM method. However, the relative positions of the first and third quartile to the median clearly indicates that the TV-based method produces mass distributions that are more symmetrical than the WDM method. Additionally, it is evident that the mass distributions obtained with the TV-based method are more consistent with each other than those obtained with the WDM method (see also Figure 13 in Appendix E). This is an important observation, as it aligns with expectations for experiment conducted in identical conditions. At last, the mass spread is lower for the TV-based method than for the WDM method (from 2.8% to 22.7%), indicating that the measured masses belong to a more compact interval, and thus, the mass resolution is necessarily better. It is noteworthy that experiment 10 does not have similar number of detected particles in the range $[40, 150]$ MDa for both methods. This discrepancy is once again explained by the property of the TV-based method, which naturally removes masses computed from the resonance frequency discontinuities mostly affected by noise and drifts.

2) Drift influence

We now present some results indicating that accounting for drifts in the denoising process for NEMS signals is necessary. To this aim, we selected two experiments among the 17 where the resonance frequencies are significantly affected by drifts, compared with another reference experiment where drifts do not seem to be present. It is noteworthy that these two experiments are different than those presented previously since they were the last conducted (Experiment 16 and Experiment 17). In the following, we analyze the results for the Experiment 17 only, but conclusions for the Experiment 16, which are similar to those presented here, can be found in Appendix D. As shown in Figure 8, Experiment 16 exhibits a larger relative deviation of the first resonance frequency: We observe a relative difference of approximately one order of magnitude. Note that the same occurs for the second resonance frequency but, for simplicity, we choose not to show it in this report.

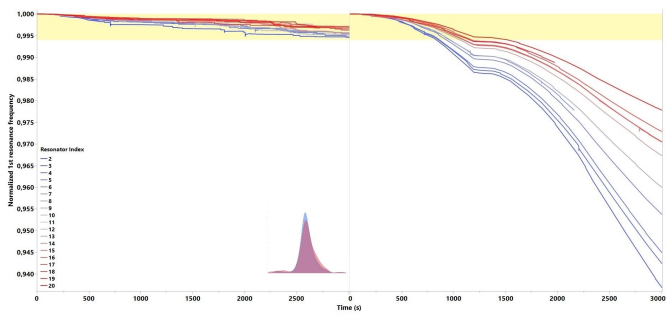

FIGURE 8. **Normalized first resonance frequencies of the NEMS for two different CLP mass measurement experiments. Left: Experiment with small drifts. Right: Experiment with large drifts. Note that the first NEMS is not shown because it was not functional in one experiment. The left image shows data with typical resonance frequency decay, producing similar mass density kernels for both the TV-based (light blue curve in the inset, 195 mass events) and WDM methods (light red curve in the inset, 205 mass events). The yellow band provides a visual cue to easily compare both situations.**

We present in Figure 9, the mass kernel densities obtained by the TV-based method and the WDM method in this case

of prominent drifts in the recorded NEMS resonance frequencies.

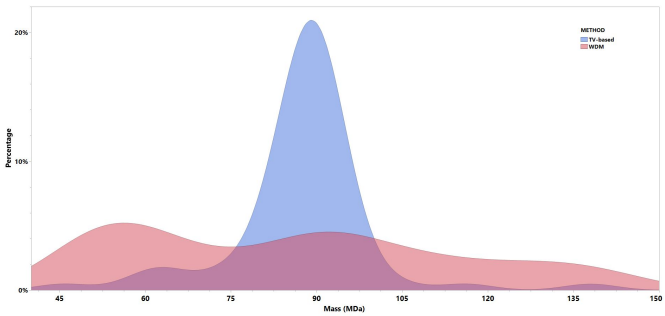

FIGURE 9. Density kernels of mass measurements in the range [40, 150] MDa for the TV-based method (light blue) and the WDM method (light red). The y-axis represents the percentage of the total number of masses in the bins of the underlying histogram, with a bin size is set to 3.75 MDa.

With Figure 9, we observe that both kernel densities have mass means close to each other (87.4 MDa for the TV-based method and 85.9 for the WDM method) which are also close to the estimated virophage mass. Interestingly, the TV-based method produces a kernel density which can be interpreted as representing true mass depositions corresponding to particles, whereas the WDM method does not reveal any signal that could be interpreted as such. This observation is attributed to the difference in the standard deviation values, which are 11.92 MDa with 68 mass events for the TV-based method and 28.58 MDa with 233 mass events for the WDM method, respectively. The difference in the number of detected masses demonstrates once again the capability of the TV-based method to remove information that are affected mostly by noise and drifts while keeping the information corresponding to the virophage capsids. Also note that the difference in the number of events (165) does not fully explain the difference in events in the mass interval $[40, 150]$ MDa reported in Figure 6, which is 382. Although this accounts for a significant portion of the overall event difference, it indicates that the TV-based method also contributes to enhancing the quality of mass estimation, even in cases where drifts are not prominent in the NEMS resonance frequencies. Similarly, it important to note that the mass kernel density produced by the WDM method in the context of large drifts contributes to the left tail observed in Figure 6. Thus, it seems that the drifts in resonance frequencies are responsible for the observed loss of signal-to-noise ratio, and that a signal processing, such as the one proposed in the present report, is necessary to keep the noise background in mass histograms at low levels. Finally, Figure 9 seems to show that the observed drifts increase with the resonator number. Since the latter is directly related to the length of the beams constituting the NEMS (the smaller the number, the longer the beam), it may indicate that drifts are correlated with the surface states of the NEMS. This assumption, similar to the one formulated with the AuNPs experiments, has not been investigated yet but will be studied in the near future.

VIII. CONCLUSION

The modeling proposed in this report improves the representation of the NEMS resonance frequency traces for true experimental data. In addition to random Gaussian noise, it incorporates the representation of unreported phenomena, namely, frequency drifts. As drifts induce changes in the shape of resonance frequency traces, they can negatively affect the NEMS resolution when measuring the mass of deposited particles. Consequently, we proposed modeling these drifts as sets of linear polynomials to fit experimental data and thus prevent loss of mass accuracy and resolution. We showed that this model, with a novel and adequate algorithm based on the Total Variation method, provides better mass accuracy and resolution properties, and an improved signal-to-noise ratio on experimental data compared to the reference method, thus underlining the importance of modeling drifts to obtain consistent mass estimates. Additionally, by providing quantitative measurements of the drifts' main features, this model offers the opportunity to obtain a deeper comprehension of NEMS physics under experimental conditions. Then, we assumed that drifts are the consequence of a continuous (in space and time) solvent droplet deposition on the NEMS surface, and tested this hypothesis against our experimental results. If the data do not show clear evidence for this deposition model, they seem to indicate that there is a link either between the initial experimental conditions and the drift slope distribution or the surface state of the NEMS.

Our future work on NEMS will focus on two main points. First, we will conduct additional mass measurement experiments to fully assess our hypothesis of continuous solvent droplet deposition on NEMS. Through this, we hope to gain a deeper understanding of the factors influencing NEMS frequencies during particle deposition. Even if our model is proven to be erroneous, these data could still highlight phenomena that have not been explored in this report. Second, in connection with the previous topic, we will explore the drift potential to predict the wear of the NEMS over time. As a potential marker of the NEMS surface state, drifts could be used as a tool to identify defective devices and consequently contribute to increase the robustness of our mass measurements. In the longer term, it could also be interesting to test artificial intelligence to improve certain aspects of our algorithm. Such elements could build upon the propositions presented in [35] and [36], where the sequential denoising methodology aligns with what we propose here. In particular, the trace feature identification part could greatly benefit from the properties of the wavelets used in [36]; the multi-scale nature of wavelets lends itself quite naturally to the separation of discontinuities, drifts, and noise.

APPENDIX A
"ELLIPSE METHOD": A STATISTICAL TEST

First, we define a statistical test under classical assumptions. Once defined, we relate this test to the "ellipse method", the definition of which is rewritten here for the sake of

completeness. Note that all notations used here are identical to those described in the main part of this report.

A. "ELLIPSE METHOD" DESCRIPTION

As mentioned in the main part of this article, the "ellipse method" described in [6] discriminates discontinuities in resonance frequency traces due to particle depositions from discontinuities due to random noise. For ease of reading, we rewrite the three steps that constitute it:

1) The first step consists of recording the first NEMS resonance frequency $\mathbf{s}^1$ and the second NEMS resonance frequency $\mathbf{s}^2$ when no particle deposition occurs to directly probe the noise affecting the NEMS resonance frequency traces during the experiments.
2) The second step is to draw a scatter plot of $\nabla\mathbf{s}^2$ with respect to $\nabla\mathbf{s}^1$, where $\nabla\mathbf{s}^i$ for $i = 1, 2$ is defined as all differences of $\mathbf{s}^i$ consecutive values. Once the scatter plot has been drawn, it is fitted with a bi-variate Gaussian distribution, thus defining an ellipse encapsulating points only owing to noise.
3) The final step is the true identification part. While recording NEMS signals when the particle deposition experiment is conducted, both $\nabla\mathbf{s}^1$ and $\nabla\mathbf{s}^2$ are computed and drawn on the previous scatter plot. If one of the newly acquired points lies inside the previously defined ellipse (up to a user defined threshold), it is not attributed to particle deposition but to noise effects. Conversely, if the newly acquired point lies outside the ellipse, it is attributed to particle deposition and is thus flagged as such.

B. χ^2_2 STATISTICAL TEST

The noise affecting both NEMS resonance frequency variables at time i is modeled as a random Gaussian variable $\boldsymbol{\epsilon}_i$, with mean equal to $\mathbf{0} \in \mathbb{R}^2$, and covariance matrix equal to a given matrix $\boldsymbol{\Sigma} \in \mathbb{R}^{2\times 2}$. Moreover, it is also modeled such that $\boldsymbol{\epsilon}_i$ and $\boldsymbol{\epsilon}_j$ are independent for all $i \neq j$. We denote d_i as a random variable built from the noise difference:

$$d_i := \boldsymbol{\epsilon}_{i+1} - \boldsymbol{\epsilon}_i$$

Consequently, d_i is a Gaussian random variable with mean $\mathbf{0} \in \mathbb{R}^2$, and covariance matrix $\bar{\boldsymbol{\Sigma}} := 2\boldsymbol{\Sigma} \in \mathbb{R}^2$. Note that d_i and d_j are also independent for all $i \neq j$. Let denote s_i as a random variable that is, at time i, the sum of the noise and the differences of both resonance frequencies:

$$s_i = \begin{pmatrix} \left(\nabla\mathbf{s}^1\right)_i \\ \left(\nabla\mathbf{s}^2\right)_i \end{pmatrix} + d_i$$

At last, we define the statistics y_i as:

$$y_i := \left\langle s_i, \bar{\boldsymbol{\Sigma}}^{-1} s_i \right\rangle_2$$

We observe that when no particle deposition occurs at time i, we have $\left(\nabla\mathbf{s}^j\right)_i = 0$ for $j = 1, 2$ and thus y_i depends only on d_i. Because d_i follows a Gaussian law $\mathcal{N}\left(\mathbf{0}, \bar{\boldsymbol{\Sigma}}\right)$, we deduce that y_i follows a χ^2 law with two degrees of freedom (also denoted χ^2_2 law), and does not depend on time i.

Conversely, when a particle deposition occurs at time i, there is a vector $\boldsymbol{\mu} \in \mathbb{R}^2$ such that $\left(\nabla\mathbf{s}^j\right)_i = \mu_j$ for $j = 1, 2$. Variable y_i then follows a non-central χ'^2_2 distribution with a noncentrality parameter λ:

$$\lambda := \sum_{i=1}^{2} \left(\bar{\boldsymbol{\Sigma}}^{-\frac{1}{2}} \boldsymbol{\mu}\right)_i^2$$

It then appears that we can define a statistical test to determine whether a measured point is due to noise only. The idea is to check for this point if λ can be considered equal to 0 or equivalently if y_i can be considered to follow a χ^2_2 law.

To this end, we define the null hypothesis H_0 as "y_i follows a χ^2_2 distribution" and a rejection area $R \subset \mathbb{R}$. Then, H_0 is rejected if, for the realization y of y_i, we have $y \in R$. In addition, we can estimate the probability of a Type I error, which is equal to $P(y_i \in R)$. Because y_i is a real non-negative random variable, the rejection area is an interval:

$$R := [\delta, +\infty[$$

where δ can be any real non-negative number.

According to the definition of y_i, there is a realization set for the random variable d_i which corresponds to this rejection area. This set, denoted $\mathcal{S}$, verifies the following:

$$\mathcal{S} := \left\{\mathbf{s} \in \mathbb{R}^2 \mid \left\langle \mathbf{s}, \bar{\boldsymbol{\Sigma}}^{-1}\mathbf{s} \right\rangle_2 \geq \delta\right\}$$

Because matrix $\bar{\boldsymbol{\Sigma}}^{-1}$ is non degenerated, $\mathcal{S}$ is thus an area located outside an ellipse described by the equation:

$$\left\langle \mathbf{s}, \bar{\boldsymbol{\Sigma}}^{-1}\mathbf{s} \right\rangle_2 = \delta$$

Choosing a suitable δ depends only on the significance level $\alpha \in \mathbb{R}$ that a user wants to obtain. Indeed, δ is always greater than or equal to the corresponding critical value.

C. THE "ELLIPSE METHOD" AS χ^2_2 STATISTICAL TEST

With all the previous developments, we can now understand why the "ellipse method" can be viewed as a statistical test. The first and second steps of the "ellipse method" are used to estimate the covariance matrix $\bar{\boldsymbol{\Sigma}}$. The user threshold in the third step corresponds to the previously introduced δ parameter. Finally, the "ellipse" corresponds to the complementary set of rejection area R. But by sticking to the previous statistical framework, we are now able to give additional information to the ones provided by the "ellipse method": In particular, we can now easily estimate the corresponding Type I Error.

APPENDIX B
PROXIMAL METHODS: APPLICATION

In this section, we briefly recall the application framework and principal properties of proximal methods. We then focus on their applications in the main steps of our denoising model.

A. PROXIMAL METHODS

Proximal methods (or the proximal gradient methods) are used to solve non-differentiable convex optimization problems. In particular, they are perfect tools for finding the argument of minimum of optimization problems of the following form:

$$\hat{\mathbf{u}} := \arg\min_{\mathbf{u}\in\mathbb{U}} f(\mathbf{u}) + g(\mathbf{u})$$

where $\mathbb{U}$ is a given space, f is a continuously differentiable function with a Lipschitz continuous gradient, and g is (possibly) a non-differentiable but convex function.

It can be proved (see for instance [15]) that under the previous hypotheses, $\hat{\mathbf{u}}$ verifies for any positive integer t:

$$\hat{\mathbf{u}} = \mathrm{Prox}^t(g)\left((\mathbf{Id} - t\partial f)(\hat{\mathbf{u}})\right)$$

In the previous equation, ∂ is the gradient operator and $\mathrm{Prox}^t(g)(\mathbf{v})$ is the proximal operator for $\mathbf{v}$ i.e. the unique solution of the equation:

$$\mathrm{Prox}^t(g)(\mathbf{v}) = \arg\min_{\mathbf{w}\in\mathbb{U}} g(\mathbf{w}) + \frac{1}{2t}||\mathbf{w}-\mathbf{v}||_2^2 \qquad (7)$$

In fact, $\hat{\mathbf{u}}$ is a fixed point and can be computed by applying the following two-step algorithm:

Algorithm 2 Compute $\hat{\mathbf{u}}$ as the fixed point of:

$j \leftarrow 0$
$\mathbf{x}^j \leftarrow x^0$
repeat
  $\mathbf{y}^j \leftarrow \mathbf{x}^j - t(\partial f)(\mathbf{x}^j)$
  $\mathbf{x}^{j+1} \leftarrow \arg\min_{\mathbf{w}\in\mathbb{U}} g(\mathbf{w}) + \frac{1}{2t}||\mathbf{w}-\mathbf{y}^j||_2^2$
  $j \leftarrow j+1$
until convergence is reached
$\hat{\mathbf{u}} \leftarrow \mathbf{x}^j$

The first step of this algorithm is a classical step for descent algorithms, in which the descent direction is the gradient of f at point $\mathbf{x}^j$. The second step involves applying the proximal operator to the result obtained in the first step. In general cases, this proximal operator is not known explicitly and must be computed numerically using iterative methods in Equation (7). The consequence is an additional computational cost (see [23]), which can negate the benefits of using such a simple approach. Nevertheless, we show in the following that, for our application, all required proximal operators are explicit, providing inexpensive and efficient methods to denoise resonance frequency traces.

Remark 10. *Note that the previous algorithm is very similar to the well-known projection-gradient method. In the latter case, a projection operator is applied after the descent-direction step, whereas in the present case, a proximal operator is used instead. Somehow, proximal operators are generalizations of projection operators.*

B. DENOISING METHOD: FIRST STEP

In this section, we focus on Equations (4), which require projection algorithms to be solved. As a by-product, we have to define a single projection operator Proj from $\mathbb{R}^{n_1}$ onto $\mathbb{G}^1$, because we project onto the same space for both resonance frequency traces. This projection operator verifies for every $\mathbf{v} \in \mathbb{R}^{n_1}$:

$$(\mathrm{Proj}(\mathbf{v}))_j := \begin{cases} \min(\mathbf{v}_j, 0) & \text{if } j \in \mathbb{I}_{\mathbb{G}^1} \\ \mathbf{v}_j & \text{if } j \notin \mathbb{I}_{\mathbb{G}^1} \end{cases} \qquad (8)$$

C. DENOISING METHOD: SECOND STEP

In this section, we consider Problems (5). These problems verify the framework of the proximal methods when we set for every resonance frequency $i = 1, 2$:

$$f(\mathbf{u}) := \frac{1}{2}||\mathbf{W}^i\mathbf{u}^i - \tilde{\mathbf{f}}^i||_2^2 - \frac{1}{\lambda_i}\sum_{j\in\mathbb{I}_{\mathbb{G}^1}} \mathbf{u}_j^i$$

$$g(\mathbf{u}) := \frac{1}{\lambda_i}||\mathbf{L}^1\mathbf{D}^1\mathbf{u}^i||_1 + \mathrm{Ind}(\mathbb{G}^1)$$

where $\mathrm{Ind}(\mathbb{G}^1)$ is the indicator function of the closed convex set $\mathbb{G}^1$.

Observe that in the previous equations, we split the L^1 term of Equation (5) into two contributions. The first one is dedicated to the trace discontinuities only (the second term of the right member in f), and the second one is attached to drifts only (the first term of the right member in g). Because the traces are functions of $\mathcal{D}^1$ and are represented by vectors in $\mathbb{D}^1$, the contribution of traces discontinuities can be simplified into linear terms. Consequently, it can be integrated into the smooth function f without modifying its differentiability.

Considering this observation, the proximal operator $\mathrm{Prox}^{\lambda_i,t}$ is defined for every $\mathbf{v} \in \mathbb{R}^{n_1}$ as:

$$\mathrm{Prox}^{\lambda_i,t}(\mathbf{v}) = \arg\min_{\mathbf{w}\in\mathbb{G}^1} \frac{1}{\lambda_i}||\mathbf{L}^1\mathbf{D}^1\mathbf{w}||_1 + \frac{1}{2t}||\mathbf{w}-\mathbf{v}||_2^2$$

Because the matrices $\mathbf{L}^1$ and $\mathbf{D}^1$ are diagonal, this equation can be rewritten as:

$$\mathrm{Prox}^{\lambda_i,t}(\mathbf{v}) := \arg\min_{\mathbf{w}\in\mathbb{G}^1} T_0(\mathbf{w},\mathbf{v}) + T_1(\mathbf{w},\mathbf{v}) + T_2(\mathbf{w},\mathbf{v})$$

Where we have set:

$$T_0(\mathbf{w},\mathbf{v}) := \frac{1}{2t}(\mathbf{w}_1 - \mathbf{v}_1)^2$$

$$T_1(\mathbf{w},\mathbf{v}) := \sum_{j\in\mathbb{I}_{\mathbb{G}^1}} \frac{1}{2t}(\mathbf{w}_j - \mathbf{v}_j)^2$$

$$T_2(\mathbf{w},\mathbf{v}) := \sum_{\substack{j\notin\mathbb{I}_{\mathbb{G}^1} \\ j\neq 1}} \frac{\mathbf{L}^1_{jj}}{\lambda_i}|\mathbf{w}_j| + \frac{1}{2t}(\mathbf{w}_j - \mathbf{v}_j)^2$$

Because all the components are independent, it is easy to obtain an explicit expression for $\text{Prox}^{\lambda_i,t}(\mathbf{v})$:

$$\text{Prox}^{\lambda_i,t}(\mathbf{v}) := \begin{cases} \mathbf{v}_j & \text{if } j = 1 \\ \min(0, \mathbf{v}_j) & \text{if } j \in \mathbb{I}_{\mathbb{G}^1} \\ \text{sign}(\mathbf{v}_j)\max(|\mathbf{v}_j| - \frac{t\mathbf{L}^1_{jj}}{\lambda_i}, 0) & \text{otherwise} \end{cases}$$

where $\text{sign}(x)$ is equal to 1 if $x \geq 0$ and -1 if $x < 0$.

Note that operators $\text{Prox}^{\lambda_i,t}$ consider the discontinuity modeling as well as the drift modeling.

D. DENOISING METHOD: THIRD STEP

Here, we focus on the minimization Problem (6). As stated, this problem is divided into two partially convex subproblems, each requiring a proximal or projection operator. In this section, we describe how to obtain an explicit expression for each of these operators.

Following the proofs in Appendix C, we first design the proximal operator associated with Equation (10). In this case, for variable $\mathbf{u} := (\mathbf{u}^1, \mathbf{D}^1\mathbf{u}^2)$, the functions f and g are equal to:

$$\begin{aligned} f(\mathbf{u}) &:= R^{\mathbf{\Phi}}\left(\mathbf{u}^1, \mathbf{D}^1\mathbf{u}^2\right) \\ g(\mathbf{u}) &:= S^{\mathbf{\Phi}}(\mathbf{u}^1, \mathbf{D}^1\mathbf{u}^2) + \text{Ind}^{\mathbf{u}^1}(\mathbb{G}^1)\text{Ind}^{\mathbf{u}^2}(\mathbb{G}^1) \end{aligned}$$

Where $\text{Ind}^{\mathbf{u}^i}(\mathbb{G}^1)$ is the indicator function of $\mathbb{G}^1$ for variable $\mathbf{u}^i$ and we have set:

$$\begin{aligned} R^{\mathbf{\Phi}}\left(\mathbf{u}^1, \mathbf{D}^1\mathbf{u}^2\right) &:= Q^{\mathbf{\Phi}}\left(\mathbf{u}^1, \mathbf{D}^1\mathbf{u}^2\right) - \sum_{j \in \mathbb{I}_{\mathbb{G}^1}} (1 + \mathbf{\Phi}_{jj})\mathbf{u}^1_j \\ S^{\mathbf{\Phi}}\left(\mathbf{u}^1, \mathbf{D}^1\mathbf{u}^2\right) &:= ||\mathbf{L}^1\mathbf{D}^1\mathbf{u}^1||_1 + ||\mathbf{L}^1\mathbf{D}^1\mathbf{u}^2||_1 \end{aligned}$$

As in the previous section, we split the L^1 term in (6) into two contributions and dispatch them according to their regularity. Observe that we considered System (1), which couples the discontinuities between both resonance frequencies. Consequently, the proximal operator $\text{Prox}^{\mathbf{u},t}$ associated with function g is written for every $(\mathbf{v}^1, \mathbf{v}^2) \in \mathbb{R}^{n_1} \times \mathbb{R}^{n_1}$ as follows:

$$\begin{aligned} \text{Prox}^{\mathbf{u},t}(\mathbf{v}^1, \mathbf{v}^2) = \underset{(\mathbf{w}^1, \mathbf{w}^2) \in \mathbb{G}^1 \times \mathbb{G}^1}{\arg\min} \; & S^{\mathbf{\Phi}}\left(\mathbf{w}^1, \mathbf{D}^1\mathbf{w}^2\right) \\ & + \frac{1}{2t}||(\mathbf{w}^1, \mathbf{w}^2) - (\mathbf{v}^1, \mathbf{v}^2)||_2^2 \end{aligned}$$

It is clear that the variables $\mathbf{v}^1$ and $\mathbf{v}^2$ are both independent in the previous expression. This leads to the following expression for the proximal operator:

$$(\text{Prox}^{\mathbf{u},t}(\mathbf{v}^1, \mathbf{v}^2))_j := \begin{cases} (\mathbf{v}^1_j, \mathbf{v}^2_j) & \text{if } j = 1 \\ (\min(\mathbf{v}^1_j, 0), \min(\mathbf{v}^2_j, 0)) & \text{if } j \in \mathbb{I}_{\mathbb{G}^1} \\ (\mathcal{T}^j(\mathbf{v}^1_j), \mathcal{T}^j(\mathbf{v}^2_j)) & \text{otherwise} \end{cases}$$

with $\mathcal{T}^j(x) := \text{sign}(x)\max(|x| - t\mathbf{L}^1_{jj}, 0)$.

An appropriate operator must be defined to solve Problem (12). As shown in Appendix C, this problem is only quadratic, and as such, we only need to define a projection operator for matrix $\mathbf{\Phi}$, or equivalently for the vector $\mathbf{y} := \mathbf{J}^1\mathbf{u}^1\mathbf{\Phi}$ introduced in (13). With $\mathbf{\Phi}$ belonging to $\mathbb{H}$, it is straightforward to define the correct projection operator $\text{Proj}^{\mathbf{\Phi}}$ for variable $\mathbf{y}$ as:

$$(\text{Proj}^{\mathbf{\Phi}}\mathbf{y})_j := \max(0, \min(\mathbf{y}_j, \Phi_{\max}\mathbf{u}^1_j))$$

APPENDIX C
NONLINEAR MODEL: CONVERGENCE PROPERTIES

In this section, we focus on proving that Algorithm 1 converges towards a local minimum of Equation (6). To this end, we show that we can generate a minimization sequence for an "uncoupled" version of (6). Classical arguments of convergence for solutions can then be applied because our solutions belong to finite-dimensional spaces. Note that the notations are identical to those defined in the main part of this report.

A. MINIMIZATION PROBLEM FOR COUPLED TRACES

We begin by recalling the functional U whose a minimizer $(\mathbf{u}^1, \mathbf{u}^2)$ has to be obtained in space $\mathbb{G}^1 \times \mathbb{G}^1$, under the constraint $\mathbf{u}^2 = \mathbf{\Phi}\mathbf{u}^1$ with $\mathbf{\Phi} \in \mathbb{H}$:

$$\begin{aligned} U(\mathbf{u}^1, \mathbf{u}^2) &:= ||\mathbf{L}^1\mathbf{u}^1||_1 + ||\mathbf{L}^1\mathbf{u}^2||_1 + Q_1(\mathbf{u}^1) + Q_2(\mathbf{u}^2) \\ Q_1(\mathbf{u}^1) &:= \frac{\lambda_1}{2}||\mathbf{W}_1\mathbf{u}^1 - \tilde{\mathbf{f}}^1||_2^2 \\ Q_2(\mathbf{u}^2) &:= \frac{\lambda_2}{2}||\mathbf{W}_2\mathbf{u}^2 - \tilde{\mathbf{f}}^2||_2^2 \end{aligned} \tag{9}$$

To explicitly consider the constraint on space $\mathbb{G}^1$, we split the unknown $\mathbf{u}^2$ into its discontinuity part, $\mathbf{J}^1\mathbf{u}^2$ and its drift part $\mathbf{D}^1\mathbf{u}^2$. Consequently, the L^1 and L^2 terms attached to $\mathbf{u}^2$ in the previous minimization problem can be rewritten in an uncoupled form (up to constant terms because they do not play any role in minimizing functional U):

$$||\mathbf{L}^1\mathbf{u}^2||_1 = ||\mathbf{L}^1\mathbf{J}^1\mathbf{u}^2||_1 + ||\mathbf{L}^1\mathbf{D}^1\mathbf{u}^2||_1$$

$$\begin{aligned} Q_2(\mathbf{u}^2) = & \frac{\lambda_2}{2}\left\langle \begin{pmatrix} \mathbf{A}_2 & \mathbf{A}_2 \\ \mathbf{A}_2 & \mathbf{A}_2 \end{pmatrix} \begin{pmatrix} \mathbf{J}^1\mathbf{u}^2 \\ \mathbf{D}^1\mathbf{u}^2 \end{pmatrix}, \begin{pmatrix} \mathbf{J}^1\mathbf{u}^2 \\ \mathbf{D}^1\mathbf{u}^2 \end{pmatrix} \right\rangle_2 \\ & - \frac{\lambda_2}{2}\left\langle \begin{pmatrix} \mathbf{A}_2\tilde{\mathbf{f}}_2 \\ \mathbf{A}_2\tilde{\mathbf{f}}_2 \end{pmatrix}, \begin{pmatrix} \mathbf{J}^1\mathbf{u}^2 \\ \mathbf{D}^1\mathbf{u}^2 \end{pmatrix} \right\rangle_2 \end{aligned}$$

Where we have set:

$$\mathbf{A}_2 := \mathbf{W}_2^T\mathbf{W}_2$$

With this formulation, we are now able to explicitly introduce nonlinear relation (1), which links the discontinuities of both resonance frequencies. By denoting $\mathbf{\Phi}$ as a diagonal matrix whose diagonal elements are either equal to 0 or equal to a scalar in $[0, \phi_i]$ at the i^{th} discontinuity location, we have:

$$||\mathbf{L}^1\mathbf{u}^2||_1 = ||\mathbf{L}^1\mathbf{J}^1\mathbf{\Phi}\mathbf{u}^1||_1 + ||\mathbf{L}^1\mathbf{D}^1\mathbf{u}^2||_1$$

$$Q_2(\mathbf{u}^2) := \frac{\lambda_2}{2}\left\langle \mathbf{Q}^{\mathbf{\Phi}}\begin{pmatrix} \mathbf{u}^1 \\ \mathbf{D}^1\mathbf{u}^2 \end{pmatrix} - \begin{pmatrix} \mathbf{f}_1^{\mathbf{\Phi}} \\ \mathbf{f}_2^{\mathbf{\Phi}} \end{pmatrix}, \begin{pmatrix} \mathbf{u}^1 \\ \mathbf{D}^1\mathbf{u}^2 \end{pmatrix} \right\rangle_2$$

where we have set:

$$\mathbf{Q}^{\mathbf{\Phi}} := \begin{pmatrix} \mathbf{\Phi}^T(\mathbf{J}^1)^T\mathbf{A}_2\mathbf{J}^1\mathbf{\Phi} & \mathbf{\Phi}^T(\mathbf{J}^1)^T\mathbf{A}_2 \\ \mathbf{A}_2\mathbf{J}^1\mathbf{\Phi} & \mathbf{A}_2 \end{pmatrix}$$
$$\begin{pmatrix} \mathbf{f}_1^{\mathbf{\Phi}} \\ \mathbf{f}_2^{\mathbf{\Phi}} \end{pmatrix} := \begin{pmatrix} \mathbf{\Phi}^T(\mathbf{J}^1)^T\mathbf{A}_2\tilde{\mathbf{f}}_2 \\ \mathbf{A}_2\tilde{\mathbf{f}}_2 \end{pmatrix}$$

It is worth noting that because both matrices $\mathbf{\Phi}$ and $\mathbf{J}^1$ are diagonal, they are commuting matrices. A similar observation holds between $\mathbf{\Phi}$ and $\mathbf{u}^1$ as long as we see the latter as a diagonal matrix whose diagonal coefficients are equal to $\mathbf{u}^1$ components. Both these remarks enable us to reformulate the previous quadratic form in two different ways. If we wish to highlight $\mathbf{u}^1$ and $\mathbf{D}^1\mathbf{u}^2$ as true variables, the quadratic form Q_2 can be expressed such that its associated matrix depends solely on $\mathbf{\Phi}$. In this scenario, $\mathbf{\Phi}$ plays a role similar to a parameter. Similarly, if $\mathbf{\Phi}$ is regarded as a true variable, it is preferable to express Q_2 as a quadratic form, with its associated matrix depending solely on $\mathbf{u}^1$ and $\mathbf{D}^1\mathbf{u}^2$.

Following this observation, we denote $Q^{\mathbf{\Phi}}$ as a quadratic form equal to Q_2 when $\mathbf{u}^1$ and $\mathbf{D}^1\mathbf{u}^2$ are variables and $\mathbf{\Phi}$ is a parameter. Its associated symmetric matrix is $\mathbf{Q}^{\mathbf{\Phi}}$, and its linear component is vector $\left(\mathbf{f}_1^{\mathbf{\Phi}}, \mathbf{f}_2^{\mathbf{\Phi}}\right)^T$. In the case where $\mathbf{\Phi}$ is a variable and $\mathbf{u}^1$ and $\mathbf{D}^1\mathbf{u}^2$ are parameters, we denote $Q^{\mathbf{u}^1\mathbf{D}^1\mathbf{u}^2}$ as the corresponding quadratic form equal to Q_2. It is characterized by its associated symmetric matrix $\mathbf{Q}^{\mathbf{u}^1\mathbf{D}^1\mathbf{u}^2}$, linear component $\mathbf{f}^{\mathbf{u}^1\mathbf{D}^1\mathbf{u}^2}$, and constant part $\mu^{\mathbf{u}^1\mathbf{D}^1\mathbf{u}^2}$ which verify the following equations:

$$\begin{aligned} \mathbf{Q}^{\mathbf{u}^1\mathbf{D}^1\mathbf{u}^2} &:= (\mathbf{u}^1)^T(\mathbf{J}^1)^T\mathbf{A}_2\mathbf{J}^1\mathbf{u}^1 \\ \mathbf{f}^{\mathbf{u}^1\mathbf{D}^1\mathbf{u}^2} &:= (\mathbf{u}^1)^T(\mathbf{J}^1)^T\left(\mathbf{A}_2\tilde{\mathbf{f}}_2 - 2\mathbf{A}_2\mathbf{D}^1\mathbf{u}^2\right) \\ \mu^{\mathbf{u}^1\mathbf{D}^1\mathbf{u}^2} &:= \left\langle \mathbf{A}_2\left(\mathbf{D}^1\mathbf{u}^2 - \tilde{\mathbf{f}}_2\right), \mathbf{D}^1\mathbf{u}^2\right\rangle_2 \end{aligned}$$

Consequently, the functional U in (9) can also be written in two different ways, depending on the variables we want to highlight.

B. MINIMIZATION PROBLEM FOR $\mathbf{U}^1$ AND $\mathbf{D}^1\mathbf{U}^2$

In this section, we focus on showing that the functional U is strictly convex when $\mathbf{u}^1$ and $\mathbf{D}^1\mathbf{u}^2$ are used as variables and $\mathbf{\Phi}$ is considered as a fixed parameter. To this end, we use (9), in which the L^2 term is replaced by the quadratic form $Q^{\mathbf{\Phi}}$. The functional U with these hypotheses can be rewritten as follows:

$$U(\mathbf{u}^1, \mathbf{u}^2) := L^{\mathbf{\Phi}}(\mathbf{u}^1, \mathbf{D}^1\mathbf{u}^2) + Q^{\mathbf{\Phi}}\left(\mathbf{u}^1, \mathbf{D}^1\mathbf{u}^2\right) \quad (10)$$

Where we have set:

$$\begin{aligned} L^{\mathbf{\Phi}}(\mathbf{u}^1, \mathbf{D}^1\mathbf{u}^2) &:= ||\mathbf{L}^1\left(\mathbf{Id}_{n_1} + \mathbf{J}^1\mathbf{\Phi}\right)\mathbf{u}^1||_1 + ||\mathbf{L}^1\mathbf{D}^1\mathbf{u}^2||_1 \\ Q^{\mathbf{\Phi}}\left(\mathbf{u}^1, \mathbf{D}^1\mathbf{u}^2\right) &:= \left\langle \bar{\mathbf{Q}}^{\mathbf{\Phi}}\begin{pmatrix} \mathbf{u}^1 \\ \mathbf{D}^1\mathbf{u}^2 \end{pmatrix} - \begin{pmatrix} \bar{\mathbf{f}}_1^{\mathbf{\Phi}} \\ \bar{\mathbf{f}}_2^{\mathbf{\Phi}} \end{pmatrix}, \begin{pmatrix} \mathbf{u}^1 \\ \mathbf{D}^1\mathbf{u}^2 \end{pmatrix}\right\rangle_2 \end{aligned} \quad (11)$$

With the following notations:

$$\bar{\mathbf{Q}}^{\mathbf{\Phi}} := \frac{\lambda_1}{2}\begin{pmatrix} \mathbf{W}_1^T\mathbf{W}_1 & \mathbf{0} \\ \mathbf{0} & \mathbf{0} \end{pmatrix} + \frac{\lambda_2}{2}\mathbf{Q}^{\mathbf{\Phi}}$$
$$\begin{pmatrix} \bar{\mathbf{f}}_1^{\mathbf{\Phi}} \\ \bar{\mathbf{f}}_2^{\mathbf{\Phi}} \end{pmatrix} := \begin{pmatrix} \frac{\lambda_1}{2}\mathbf{W}_1^T\mathbf{W}_1\tilde{\mathbf{f}}_1 + \frac{\lambda_2}{2}\mathbf{f}_1^{\mathbf{\Phi}} \\ \frac{\lambda_2}{2}\mathbf{f}_2^{\mathbf{\Phi}} \end{pmatrix}$$

Considering $\mathbf{\Phi}$ as a known and fixed parameter, the matrix $\bar{\mathbf{Q}}^{\mathbf{\Phi}}$ in Equation (11) is well defined. In addition, we notice that it is also positive-definite. Indeed the corresponding quadratic form $Q^{\mathbf{\Phi}}$ is only a rewriting of the sum of quadratic forms Q_1 and Q_2 but for subset $\mathcal{Q}$:

$$\mathcal{Q} := \left\{\left(\mathbf{u}^1, \mathbf{u}^2\right),\ \mathbf{u}^1 \in \mathbb{G}^1,\ \mathbf{u}^2 \in \mathbb{G}^1 \text{ and } \mathbf{J}^1\mathbf{u}^2 = \mathbf{J}^1\Phi\mathbf{u}^1\right\}$$

Because the sum of Q_1 and Q_2 is trivially positive-definite over the entire space $\mathbb{G}^1$, being the sum of two positive-definite quadratic forms on two independent variables, it is also positive-definite on $\mathcal{Q}$. Consequently, the matrix $\mathbf{Q}^{\mathbf{\Phi}}$ is positive-definite as well. We can then deduce that the functional U is strictly convex in variables $\mathbf{u}^1$ and $\mathbf{D}^1\mathbf{u}^2$ as the sum of convex functions with a strictly convex quadratic form. Thus, U admits a single and global minimizer for a fixed parameter $\mathbf{\Phi}$.

C. MINIMIZATION PROBLEM FOR Φ

We are now interested in minimizing the functional U with $\mathbf{\Phi}$ as a variable, while treating $\mathbf{u}^1$ and $\mathbf{D}^1\mathbf{u}^2$ as fixed parameters. We aim to demonstrate that the corresponding minimizer is unique and global. To prove this, we use the quadratic form $Q^{\mathbf{u}^1\mathbf{u}^2}$ in Equation (9) to represent the L^2 term in U. With this in mind, we write the functional U as:

$$U(\mathbf{u}^1, \mathbf{u}^2) := L^{\mathbf{u}^1\mathbf{D}^1\mathbf{u}^2}(\mathbf{\Phi}) + Q^{\mathbf{u}^1\mathbf{D}^1\mathbf{u}^2}(\mathbf{\Phi}) \quad (12)$$

Where we have:

$$\begin{aligned} L^{\mathbf{u}^1\mathbf{D}^1\mathbf{u}^2}(\mathbf{\Phi}) :=& ||\mathbf{L}^1\left(\mathbf{Id}_{n_1} + \mathbf{J}^1\mathbf{\Phi}\right)\mathbf{u}^1||_1 + ||\mathbf{L}^1\mathbf{D}^1\mathbf{u}^2||_1 \\ Q^{\mathbf{u}^1\mathbf{D}^1\mathbf{u}^2}(\mathbf{\Phi}) :=& \frac{\lambda_2}{2}\left\langle \mathbf{Q}^{\mathbf{u}^1\mathbf{D}^1\mathbf{u}^2}\mathbf{\Phi}, \mathbf{\Phi}\right\rangle_2 \\ & - \frac{\lambda_2}{2}\left\langle \mathbf{f}^{\mathbf{u}^1\mathbf{D}^1\mathbf{u}^2}, \mathbf{\Phi}\right\rangle_2 \\ & + Q_1(\mathbf{u}^1) + \frac{\lambda_2}{2}\mu^{\mathbf{u}^1\mathbf{D}^1\mathbf{u}^2} \end{aligned}$$

We observe that some of the terms in the previous equation do not depend on $\mathbf{\Phi}$, and thus can be discarded when looking for a minimizer along the $\mathbf{\Phi}$ axis. U can then be equivalently replaced by a functional V defined in the same space but with a simpler expression:

$$\begin{aligned} V(\mathbf{u}^1, \mathbf{u}^2) :=& ||\mathbf{L}^1\mathbf{J}^1\mathbf{u}^1\mathbf{\Phi}||_1 + \frac{\lambda_2}{2}\left\langle \mathbf{Q}^{\mathbf{u}^1\mathbf{D}^1\mathbf{u}^2}\mathbf{\Phi}, \mathbf{\Phi}\right\rangle_2 \\ & - \frac{\lambda_2}{2}\left\langle \mathbf{f}^{\mathbf{u}^1\mathbf{D}^1\mathbf{u}^2}, \mathbf{\Phi}\right\rangle_2 \end{aligned}$$

Considering that jump orientations are known beforehand and that $\mathbf{\Phi}$ is a vector whose components are all non-negative because it belongs to $\mathbb{H}$, the L^1 terms in V are in fact linear terms. Consequently, minimizing functional V is equivalent to minimizing a simple quadratic form. It remains to show that

this quadratic form is strictly convex. When looking at matrix $\mathbf{Q}^{\mathbf{u}^1\mathbf{D}^1\mathbf{u}^2}$, it does not seem that it can be a positive-definite matrix. Indeed, $\mathbf{u}^1$ is a vector whose components may be equal to zero, thus preventing $\mathbf{Q}^{\mathbf{u}^1\mathbf{D}^1\mathbf{u}^2}$ from being injective and, in turn, from being positive-definite. Nevertheless, we can proceed to a change of variable to remove this apparent defect. Let denote $\mathbf{y}$ the following vector:

$$\mathbf{y} := \mathbf{J}^1\mathbf{u}^1\mathbf{\Phi} \tag{13}$$

Because we want to minimize V along the $\mathbf{\Phi}$ axis and because $\mathbf{u}^1$ is a known and fixed vector, $\mathbf{y}$ is a variable that depends linearly on $\mathbf{\Phi}$ only and belongs to a convex space $\mathcal{Y}$:

$$\mathcal{Y} := \{\mathbf{y} \in \mathbb{R}^{n_1} \mid \mathbf{y}_i \in [\mathbf{u}_i^1\phi_i, 0] \text{ if } i \in \mathbb{J}^1 \text{ and } \mathbf{y}_i = 0 \text{ otherwise}\}$$

With this change of variable, functional V can be equivalently rewritten for all $\mathbf{y} \in \mathcal{Y}$ as:

$$U(\mathbf{u}^1, \mathbf{u}^2) := ||\mathbf{L}^1\mathbf{y}||_1 + \frac{\lambda_2}{2}\left\langle \mathbf{A}_2\left(\mathbf{y} - \tilde{\mathbf{f}}_2 - 2\mathbf{D}^1\mathbf{u}^2\right), \mathbf{y}\right\rangle_2$$

In this relation, $\mathbf{A}_2$ is a positive-definite matrix which implies that V is a convex functional for variable $\mathbf{y} \in \mathcal{Y}$. We conclude that V admits a single global minimizer along the $\mathbf{y}$-axis. This minimizer is transformed into a minimizer in the $\mathbf{\Phi}$ variable. Except for the $\mathbf{u}^1$ components equal to zero, the other components of $\mathbf{\Phi}$ are computed using Equation (13) because $\mathbf{J}^1$ is a one-to-one mapping . For the $\mathbf{u}^1$ components equal to zero, the corresponding components of $\mathbf{\Phi}$ are set to ϕ_i. This is a requirement of the NEMS physics. In conclusion, functional V (and U as well) has a single global minimizer along the $\mathbf{\Phi}$ axis.

The interval to which each ϕ_i belongs remains to be defined. Because $\mathbf{\Phi}$ is designed to be equivalent to the second equation in (1), we deduce that for the i^{th} discontinuity, we have:

$$\phi_i := \frac{\mathbf{s}_i^2}{\mathbf{s}_i^1}\max_{x_i}\Phi(x_i)$$

Given that the function $\Phi(x_i)$ is known, we must estimate the ratio $\mathbf{s}_i^2$ over $\mathbf{s}_i^1$. To ensure the convergence of Algorithm 1, this ratio must be fixed once and for all. A consistent way to achieve this is by utilizing the trace values computed from Problems (5). As these trace estimates are calculated to approximate the true signals closely owing to the noise constraint, their ratio also approximates the true ratio. Using this approximated ratio, it is now straightforward to define ϕ_i.

Remark 11. *The previous change of variable also has practical consequences: Minimizing U on the variable $\mathbf{y}$ with a numerical solver becomes an easy task thanks to the projected gradient descent algorithms. These algorithms are efficient in minimizing quadratic problems even with additional convex constraints (in our case, space $\mathcal{Y}$), provided that there is an explicit projector onto these constraints. In the present case, such an expression is available. See Appendix B for further details.*

D. CONVERGENCE TOWARDS LOCAL MINIMIZER

Now that we have proved that the functional U has a single global minimizer in $(\mathbf{u}^1, \mathbf{D}^1\mathbf{u}^2)$ and $\mathbf{\Phi}$ directions, it remains to be shown that we can provide a way to simultaneously obtain a local minimizer in the three variables. First, let $U^{\mathbf{\Phi}}$ define the following functional defined for every $(\mathbf{u}^1, \mathbf{u}^2) \in \mathbb{G}^1 \times \mathbb{G}^1$:

$$U^{\mathbf{\Phi}}(\mathbf{u}^1, \mathbf{D}^1\mathbf{u}^2) := L^{\mathbf{\Phi}}(\mathbf{u}^1, \mathbf{D}^1\mathbf{u}^2) + Q^{\mathbf{\Phi}}\left(\mathbf{u}^1, \mathbf{D}^1\mathbf{u}^2\right)$$

Similarly, for every $(\mathbf{u}^1, \mathbf{u}^2)$ in $\mathbb{G}^1 \times \mathbb{G}^1$, we denote $U^{\mathbf{u}^1\mathbf{D}\mathbf{u}^2}(\mathbf{\Phi})$ as the functional defined on $\mathbb{G}^1 \times \mathbf{D}^1\mathbb{G}^1$ which is written as:

$$U^{\mathbf{u}^1\mathbf{D}^1\mathbf{u}^2}(\mathbf{\Phi}) := L^{\mathbf{u}^1\mathbf{D}^1\mathbf{u}^2}(\mathbf{\Phi}) + Q^{\mathbf{u}^1\mathbf{D}^1\mathbf{u}^2}(\mathbf{\Phi})$$

Consequently, we observe that with relations (10) and (12), the following equality holds:

$$U^{\mathbf{\Phi}}(\mathbf{u}^1, \mathbf{D}^1\mathbf{u}^2) = U^{\mathbf{u}^1\mathbf{D}^1\mathbf{u}^2}(\mathbf{\Phi}) \tag{14}$$

Now, let $\mathbf{u}^{1,n}$, $\mathbf{u}^{2,n}$ be vectors in $\mathbb{G}^1 \times \mathbb{G}^1$. Then, there is a matrix $\mathbf{\Phi}^n$ in $\mathbb{H}$ such that:

$$\mathbf{J}^1\mathbf{u}^{2,n} = \mathbf{J}^1\mathbf{\Phi}^n\mathbf{u}^{1,n}$$

Owing to the existence of a minimizer of U along $(\mathbf{u}^1, \mathbf{D}^1\mathbf{u}^2)$ axes, there are two vectors $\tilde{\mathbf{u}}^{1,n}$ and $\tilde{\mathbf{u}}^{2,n}$ both in $\mathbb{G}^1 \times \mathbb{G}^1$ which verify the following:

$$U^{\mathbf{\Phi}^n}(\tilde{\mathbf{u}}^{1,n}, \mathbf{D}^1\tilde{\mathbf{u}}^{2,n}) \leq U^{\mathbf{\Phi}^n}(\mathbf{u}^{1,n}, \mathbf{D}^1\mathbf{u}^{2,n}) \tag{15}$$

Because U admits also a minimizer along the $\mathbf{\Phi}$ axis, we deduce that there is a matrix $\mathbf{\Phi}^{n+1}$ which verifies:

$$U^{\tilde{\mathbf{u}}^{1,n}\mathbf{D}^1\tilde{\mathbf{u}}^{2,n}}(\mathbf{\Phi}^{n+1}) \leq U^{\tilde{\mathbf{u}}^{1,n}\mathbf{D}^1\tilde{\mathbf{u}}^{2,n}}(\mathbf{\Phi}^n) \tag{16}$$

Now, following the definition of $U^{\mathbf{\Phi}}$, $U^{\mathbf{u}^1\mathbf{u}^2}$ and Equation (14), we have:

$$\begin{aligned} U^{\tilde{\mathbf{u}}^{1,n}\mathbf{D}^1\tilde{\mathbf{u}}^{2,n}}(\mathbf{\Phi}^{n+1}) &= U(\tilde{\mathbf{u}}^{1,n}, \tilde{\mathbf{u}}^{2,n}) \\ U^{\tilde{\mathbf{u}}^{1,n}\mathbf{D}^1\tilde{\mathbf{u}}^{2,n}}(\mathbf{\Phi}^n) &= U^{\mathbf{\Phi}^n}(\tilde{\mathbf{u}}^{1,n}, \mathbf{D}^1\tilde{\mathbf{u}}^{2,n}) \\ U^{\mathbf{\Phi}^n}(\mathbf{u}^{1,n}, \mathbf{D}^1\mathbf{u}^{2,n}) &= U(\mathbf{u}^{1,n}, \mathbf{u}^{2,n}) \end{aligned}$$

where we have implicitly written:

$$\tilde{\mathbf{u}}^{2,n} = \mathbf{L}^1\mathbf{J}^1\mathbf{\Phi}^{n+1}\tilde{\mathbf{u}}^{1,n} + \mathbf{D}^1\tilde{\mathbf{u}}^{2,n}$$

This equalities combined with Equations (15), (16) lead to:

$$U(\tilde{\mathbf{u}}^{1,n}, \tilde{\mathbf{u}}^{2,n}) \leq U(\mathbf{u}^{1,n}, \mathbf{u}^{2,n})$$

Finally, when setting:

$$\begin{aligned} \mathbf{u}^{1,n+1} &:= \tilde{\mathbf{u}}^{1,n} \\ \mathbf{u}^{2,n+1} &:= \tilde{\mathbf{u}}^{2,n} \end{aligned}$$

We have:

$$U(\mathbf{u}^{1,n+1}, \mathbf{u}^{2,n+1}) \leq U(\mathbf{u}^{1,n}, \mathbf{u}^{2,n})$$

In other words, we produced a minimization sequence for the functional U. As we work on finite-dimensional spaces, this implies that there is a minimization sequence for U , which converges towards a local minimum represented by the vectors $\mathbf{u}^{1,*}$ and $\mathbf{u}^{2,*}$.

APPENDIX D
IMPACT OF DRIFT MODELING ON PARTICLE MASS DISTRIBUTION

This section focuses on evaluating the impact of drifts on particle mass distribution in two different ways. Firstly, it aims to determine if different drift models influence the overall particle mass distribution. This was achieved by recalculating the mass distribution profile for the two experiments involving AuNPs in this report. We accomplished this by doubling the number of linear polynomials required to represent each drift. Secondly, we provide an analysis of the mass distributions of virophage capsids from Experiment 16: In this experiment, the NEMS resonance frequencies were also affected by large drifts. This analysis complements the discussion in the main body of the report. For each scenario, we offer insights into the varied results obtained.

A. AuNPs MASS DISTRIBUTION

The main features of the recomputed particle mass distribution are listed in Table 4 and the mass distribution obtained is represented in Figure 10.

	BBI gold nanoparticles	TV based	WDM
mass mean (MDa)	151.51	151.87	162.66
mass variance (MDa)	N/A	27.61	32.92

TABLE 4. Table of mass distribution statistics for TV-based and WDM methods in the mass interval [50, 250] MDa, with BBI AuNPs as a reference. In this interval, the total number of detected particles is 312 and 308.

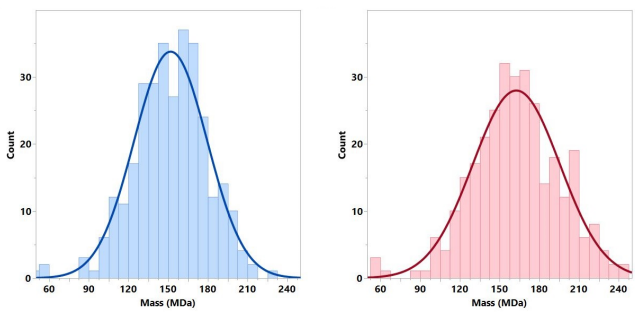

FIGURE 10. Mass distribution profile for TV-based denoising and WDM methods in the mass interval [50, 250] MDa. Bin size is equal to 7.5 MDa. In this interval, the total number of detected particles is respectively equal to 312 and 308. Left: Mass distribution profile for the TV-based denoising method. Right: Mass distribution profile for the WDM method.

We observe that there are no noticeable changes in the mass distribution profile in comparison with Figure 5. The same observation occurs in the mass distribution features, where the observed variations of the mass mean and mass variance are of the same order of magnitude as those provided in Table 1. Both results confirm that our drift modeling has marginal impacts on particle mass estimations; hence, it is a robust method to capture particle mass in the presence of drifts.

B. CLPs MASS DISTRIBUTION

We present in Figure 11 the NEMS resonance frequencies which were observed during Experiment 16.

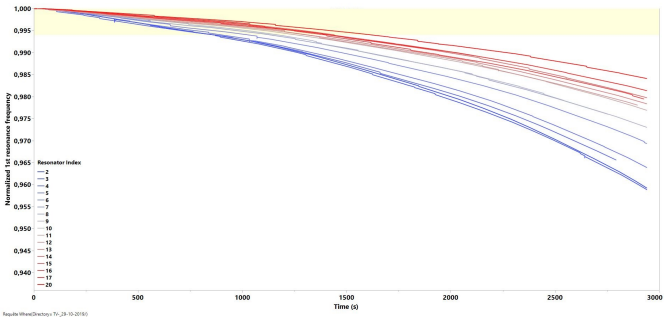

FIGURE 11. Normalized first resonance frequencies of the NEMS for CLP experiment number 16. The yellow band provides a visual cue identical to that of Figure 8, indicating the band where resonance frequencies minimally affected by drifts should be.

With Figure 11, we observe a similar decay of resonance frequencies to those observed in Experiment 17. The order of magnitude of decay is approximately 2 to 10 times the expected values for experiments where resonance frequencies are not strongly affected by drifts.

Having made this observation, we now focus on the the mass density kernels provided by the TV-based and WDM methods. When computing the mass for each discontinuity detected in the resonance frequencies, we obtained Figure 12.

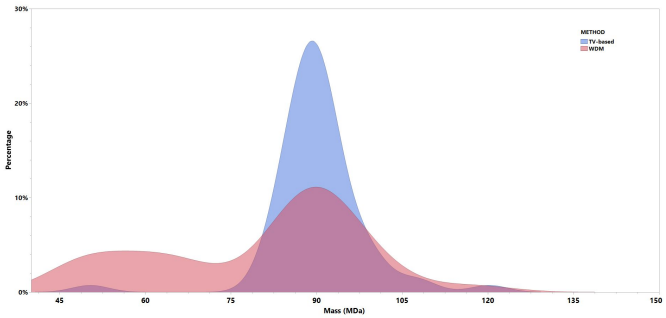

FIGURE 12. Density kernels of mass measurements in the range [40, 150] MDa for the TV-based method (light blue) and the WDM method (light red). The y-axis represents the percentage of the total number of masses in the bins of the underlying histogram, with a bin size is set to 3.75 MDa.

Again, we observe that the TV-based method produces a mass kernel density with a peak better defined than that of the WDM method. This is due to the removal of masses in the left part of the studied mass interval, which are responsible for the existence of a heavy tail in the WDM kernel density. We also note that the TV-based method detects 64 mass events in the interval $[40, 150]$ MDa, whereas the WDM method identifies 99 mass events. Although fewer that those reported in the main body of this report, this difference follows a trend similar to what is indicated in the CLPs section. Lastly, it is

noteworthy that this difference in number of events (35), even when combined with the difference reported for Experiment 17 (165), represents approximately 50% of the difference in the number of mass events reported in Figure 6. This shows that the TV-based method operates effectively not only in situation where resonance frequencies are affected by large drifts but also in more standard situations.

APPENDIX E
EXPERIMENT ANALYSIS: RESULT CONSISTENCY

In this section, we show some additional images indicating that our TV-based method produces more consistent results than the WDM method, when experiments conducted the same day are analyzed.

A. COMPLEMENTARY ILLUSTRATIONS

We recall that the following results pertain to the four consecutive experiments on the mass measurements of virophage capsids, as described in the main body of this report. To illustrate our findings, we used box plots and violon iso-responses, concluding that mass measurements are more consistent from one experiment to another when using the TV-based method. Nevertheless, these types of representations may require deeper insights to support our conclusion. Therefore, we propose additional images that could more clearly substantiate our assertion.

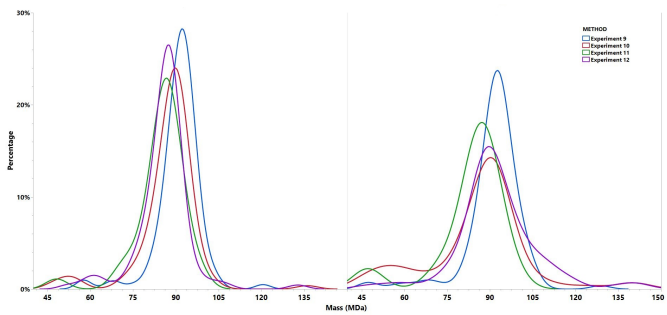

FIGURE 13. Density kernels of mass measurements in the range [40, 150] MDa for the four consecutive experiments conducted on virophage capsids. Left: TV-based method. Right: WDM method. The y-axis represents the percentage of the total number of masses in the bins of the underlying histogram, with a bin size is set to 3.75 MDa.

In Figure 13, we observe that the density kernels have higher peaks and are narrower with the TV-based method compared to the WDM method. Moreover, the widths of these density kernels are more consistent with each other when using the TV-based method than with the WDM. This is primarily due to the more symmetrical shape and the absence of heavy tail in the TV-based results. These observations are entirely consistent with the ones described in the main body of this report.

APPENDIX F
CONTINUOUS PARTICLES DEPOSITION MODELING

In this section, we present the main implications of the continuous particle deposition modeling on the behavior of NEMS. We first present the different hypotheses we use, and then present the partial derivative equations which are the core of our modeling.

A. HYPOTHESES

First, we used the same hypotheses on NEMS as in [6]. In particular, a NEMS is a homogeneous rectangular beam whose length L is much larger than its width w and thickness t. The extremal planes at $x = 0$ and $x = L$ are fixed and motionless. The lateral planes (i.e., surfaces perpendicular to the x-axis) have a constant surface S and a constant perimeter P. As long as we consider a NEMS between two consecutive particle depositions (say at time t_0 and time $t_1 > t_0$), the effective weight $M(t_0)$ of any lateral plane does not depend on x and is constant for all $t_0 \leq t \leq t_1$.

When considering solvent deposition on the NEMS, we assumed that the solvent is spatially homogeneously deposited on the NEMS, which means that between two particle depositions, the deposited linear solvent mass $m(t, t_0)$ does not depend on x, y and z. We also assumed that $m(t, t_0)$ is a summable function over time t. Finally, the NEMS was assumed to vibrate only along the y-axis, with no displacements in the other orthogonal directions, and the NEMS vibrating mode shapes are not modified by particle deposition or solvent deposition.

Finally, recall that our experiments were conducted with an array of 20 NEMS. With the technology we used, the resonance frequencies for the entire set of NEMS are identified sequentially, that is, one NEMS after another. Thus, as 20 ms is sufficient to obtain the first two resonance frequencies for a single NEMS, obtaining the resonance frequencies for all NEMS requires 400 ms. Once all the NEMS resonance frequencies are acquired, a new cycle of resonance frequency measurements is initiated to detect new potential particle depositions.

B. MODELING WITH PARTIAL DERIVATIVE EQUATIONS

According to above hypotheses, every NEMS follows the Euler-Bernoulli beam theory, which implies that its displacements $w(x, t)$ are governed by the following partial derivative equations for all $t \in [t_0, t_1]$:

$$(M(t_0) + m(t, t_0)P)\frac{\partial^2 w}{\partial t^2}(x, t) + EI\frac{\partial^4 w}{\partial x^4}(x, t) = 0$$

where E is the Young's modulus of the NEMS, and I is the inertial moment in flexion.

A solution is obtained by projecting this equation onto the function space defined by the eigenfunctions of the bilaplacian operator $\partial^4/\partial x^4$. If we denote $s_n(x)$ as these eigenfunc-

tions and λ_n as the corresponding eigenvalues, this projection operation leads to a system of linear decoupled problems (for $n \geq 1$ and for all $t \in [t_0, t_1]$):

$$(M(t_0) + m(t, t_0)P)\frac{\partial^2 \alpha_n}{\partial t^2}(t) + EI\lambda_n \alpha_n(t) = 0 \qquad (17)$$

where we have set $w(x,t) = \sum_{n=1}^{+\infty} \alpha_n(t) s_n(x)$.

Equation (17) can be recast as a matrix first-order ordinary differential equation, but where the matrix components are still dependent on time:

$$\left(\frac{\partial}{\partial t}\mathbf{x}\right)(t) = \mathbf{A}(t)\mathbf{x}(t)$$

$$\mathbf{x}(t) := \begin{pmatrix} \alpha_n \\ \frac{\partial \alpha_n}{\partial t} \end{pmatrix}(t)$$

Unfortunately, matrix $\mathbf{A}(t)$ does not possess the properties required to solve the corresponding system using classical mathematical tools. In particular, we do not have $\mathbf{A}(t_2)\mathbf{A}(t_3) = \mathbf{A}(t_3)\mathbf{A}(t_2)$ for all $(t_2, t_2) \in [t_0, t_1] \times [t_0, t_1]$. This implies that such a system must be solved numerically for a certain class of functions $g(t)$ or approximately solved with perturbations techniques. We focus on the latter to obtain ideas on how a NEMS interacts with its environment.

To simplify the computations, we assume $t_0 = 0$. This assumption is valid because a simple change of variable in (18) leads to the corresponding situation. Moreover, we also suppose that function $m(t, 0)$ writes $c(t)t$, where $c(t)$ is a function that varies slowly over time: For quite large time interval of the form $[0, t_1]$, its derivative is close to 0. In addition, we assume that we have $c(t)tP << M(0)$ for all $t \in [0, t_1]$. In terms of physics interpretation, a quasi-constant mass of solvent is continuously and slowly deposited on every NEMS.

According to these hypotheses, Equation (17) can be approximated in the first order as (for $n \geq 1$ and for all $t \in [t_0, t_1]$):

$$\frac{\partial^2 \alpha_n}{\partial t^2}(t) + \omega_{0,n}^2\left(1 - \frac{c(0)P}{M(0)}t\right)\alpha_n(t) = 0 \qquad (18)$$

where $\omega_{0,n}^2 := EI\lambda_n / M(0)$ is the n^{th} resonance pulsation of the NEMS (with our NEMS geometry, $\lambda_1/\lambda_2 = 0.602$ [6]).

With the previous hypotheses, it is possible to use perturbation methods to solve Equation (18). Thus, the true solution $\alpha_n(t)$ is split into two functions, $\alpha_n^0(t)$ and $\alpha_n^1(t)$, which verify the following system of equations:

$$\frac{\partial^2 \alpha_n^0}{\partial t^2}(t) + \omega_{0,n}^2 \alpha_n^0(t) = 0$$

$$\frac{\partial^2 \alpha_n^1}{\partial t^2}(t) + \omega_{0,n}^2 \alpha_n^1(t) + t\alpha_n^0(t) = 0$$

Where we have written:

$$\alpha_n(t) := \alpha_n^0(t) - \frac{c(0)P}{M(0)}\omega_{0,n}^2 \alpha_n^1(t)$$

Again, we recall that the previous system of equations is valid only if $c(0)P\omega_{0,n}^2 t / M(0)$ is very small; that is, for time t close to 0. However, this condition, although restrictive, fits with the acquisition time of the resonance frequencies for a single NEMS, and thus is acceptable.

We can now solve the previous system of equations. Clearly, $\alpha_n^0(t)$ is equal to a linear combination of $\cos(\omega_{0,n}t)$ and $\sin(\omega_0 t)$ which are expected functions for a NEMS not covered by a solvent layer. Once $\alpha_n^0(t)$ is known, estimating $\alpha_n^1(t)$ is straightforward, and we obtain (with A and B in $\mathbb{R}$):

$$\alpha_n^1(t) := \int_0^t s(A\cos(\omega_{0,n}s) + B\sin(\omega_{0,n}s))\sin(\omega_{0,n}(t-s))\,\mathrm{d}s$$

After linearization and integration, function α_n^1 can be explicitly written as a linear combination of $t\cos(\omega_{0,n}t)$ and $t\sin(\omega_{0,n}t)$. This implies that as long as t is sufficiently small, $\alpha_n(t)$ can be approximated well by $\alpha_n^0(t)$. This means that the solvent mass deposited during the resonance frequency measurement of a single NEMS (which lasts only 20 ms) has no effect on the resulting values. As a side effect, the resonance frequencies we obtained correspond to the resonance frequencies of a NEMS with a constant mass, equal to the sum of its own mass and the mass of solvent deposited before the measurement.

Consequently, for a particular NEMS, the difference $D_n(\Delta t)$ between two consecutive measurements for the n^{th} resonance frequency verifies at times t_0 and $t_0 + \Delta t$:

$$\begin{aligned} D_n(\Delta t) &:= \frac{\omega_{0,n}}{2\pi}(t_0 + \Delta t) - \frac{\omega_{0,n}}{2\pi}(t_0) \\ &= \frac{\sqrt{EI\lambda_n}}{2\pi}\left(\sqrt{\frac{1}{M(t_0) + c(t_0)\Delta t}} - \sqrt{\frac{1}{M(t_0)}}\right) \end{aligned}$$

where $\Delta t = 200\text{ms}$.

Considering that the added solvent mass is assumed to be largely inferior to the NEMS mass, the previous equation can be rewritten as:

$$D_n(\Delta t) = -\frac{\omega_{0,n}\, c(t_0)}{4\pi M(t_0)}\Delta t + o(\Delta t)$$

We then observe that our model of continuous solvent deposition leads to a linear decrease in both resonance frequencies between two frequency measurements (i.e., every 400 ms). This observation justifies the use of linear polynomials as drift representations. Moreover, after two particle deposition events, at times s_0 and s_1 for instance, we note that the rate of the frequency decrease $D_n(\Delta t)/\Delta t$ diminishes as $M(s_0) \leq M(s_1)$ (this remark is also valid if $c(s_0) \leq c(s_1)$). Then, we deduce that the resonance frequency decrease slows between successive particle depositions. Finally, this model

predicts a linear correlation between the resonance frequency decrease because we have:

$$\frac{D_1(\Delta t)}{D_2(\Delta t)} := \frac{\omega_{0,1}}{\omega_{0,2}} = \frac{\lambda_1}{\lambda_2} = 0.602$$

C. DRIFTS: EXPERIMENTAL VALIDATION

In this section, we attempt to extract some information from the drifts computed using our denoising model. Experimentally, we observe that drifts appear as soon as the nebulizer works. Naturally, we would think that this observation could be related to a fluid, a mix between air and the solvent in a gas state, which would exist in the chamber where the NEMS are located and would be continuously and uniformly adsorbed on the NEMS. Intuitively, this process should cause a constant decrease in the NEMS resonance frequencies between two particle deposition events. This intuition is supported by the modeling developed in the previous section, where each linear polynomial that constitutes a drift is shown to be decreasing.

This model allows us to provide qualitative trends regarding the time behavior of drifts. Thus, let us consider an experiment in which a NEMS is surrounded by a very large amount of solvent gas that is adsorbed continuously at rate $c(t)$. During the first moments of this experiment and for small $c(t)$ values, we can suppose that the amount of adsorbed solvent gas is negligible compared to the total amount of solvent gas around the NEMS. In the first-order approximation, the solvent gas concentration around the NEMS remains constant and the function $c(t)$ remains almost constant. Consequently, a single drift should boil down to a single linear polynomial defined over a long time interval. If the amount of solvent gas remains constant over time (owing to a continuous supply by the nebulization/heating processes), this state lasts until the end of the experiment, and the observed drifts appear as long straight lines. If no additional supply of solvent gas occurs in the NEMS chamber, the deposition rate $c(t)$ cannot be considered constant between two frequency measurements after a while. During this phase, the amount of adsorbed solvent gas cannot be neglected because it represents an important portion of the solvent gas surrounding the NEMS. Consequently, we should observe drifts characterized by a rapid succession of numerous linear polynomials, each defined over a short time interval. Contrary to the initial situation where a drift is similar to a straight line, a drift is then more like a broken line. Finally, when no solvent gas remains, a drift should be represented as a horizontal line over a long time interval, as no gas adsorption occurs.

Before any comparison, we must check whether the rate of particle deposition onto our NEMS array is similar to that in our two experiments. On the contrary, a higher deposition rate would mean shorter durations between two particle depositions and mechanically shorter drifts (by definition). Consequently, we need to plot the experimental cumulative distributions of detected particle-landing events over time and compare it to the cumulative distribution of landing-particle events occurring uniformly over time. The results are shown in Figure 14.

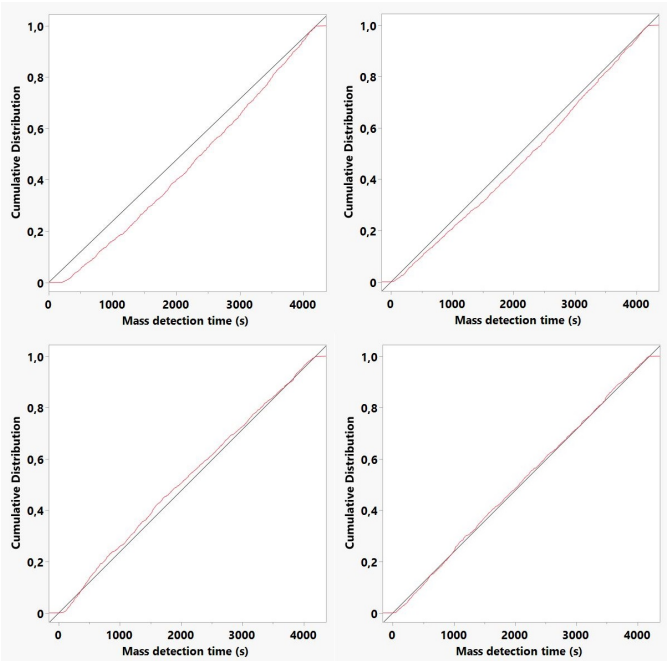

FIGURE 14. Cumulative distributions of landing-particle events. Red lines are the experimental cumulative distributions, black lines are the cumulative distributions of particle-landing events occuring uniformly in time. The first line of plots represent the landing events for the first experiment, separated according to our recording constraints (Left: data recorded from [0, 2600]*s*, Right: data recorded from [2600, 4200]*s*). The second line of plots represent the landing events for the second experiment, separated according to our recording constraints (Left: data recorded from [0, 2600]*s*, Right: data recorded from [2600, 4200]*s*). Note that all time are rescaled on the same interval to ease comparisons.

We note that the first experiment shows a difference between the experimental cumulative distribution and the expected cumulative distribution. This is essentially true for the first half of the experiment, where the time distribution of landing events shows a large deficit of events. The second experiment shows a distribution closer to a uniform distribution. As we observe a lack of particle deposition in only one recording, whereas the experimental conditions did not change during the entire experimental campaign, we attribute the observed difference to a non-homogeneity in the sample at the beginning of the experiment. In addition to the latter case, the rate of landing of particles can be considered constant in our experiments, and the observed drifts should have a similar mean duration.

Our modeling explaining drift origin is then compared with the experimental results, as shown in Figure 15. In the latter, we drew the starting time of every linear polynomial in drifts versus the size of the linear polynomials (i.e., their duration since the sampling time is constant). When removing data from the first half of the first experiment which show a different distribution, we visually observe a common pattern in data distribution: The linear polynomials constituting drifts can

be divided into three distinct populations. A population with small sizes, which is present at a high density from the beginning to the end of the data. A population with intermediary sizes and lower density, which may extend until a certain time (as in the second experiment). And a population with high sizes and low density, which is not represented after a short period. This visual impression is strengthened by a K-means clustering method that identifies the same three populations in the gathered data. The existence of such groups of data seems to be in accordance with the solvent gas adsorption modeling described above. Nevertheless, it is still insufficient, and we then take a closer look at some other quantitative information. Again, the first half of the first experiment shows a different behavior. Very small linear polynomials do not appear to be present, whereas very large linear polynomials do. These observations may be linked to the fact that fewer particles land on the NEMS. As mentioned above, less landing particles per unit of time potentially means longer drifts, and then longer linear polynomials. However, the absence of very small linear polynomials results in smoother resonance frequency traces. Apart from the different initial states of the experimental sample, we cannot provide explanations to accurately represent the obtained results.

It is interesting to note that our TV-based denoising method can expose the differences that may arise between different experiments (such as in the upper left picture in Figure 15), as well as internal structures within frequency traces that are not accessible through mere examination of the final particle mass distribution.

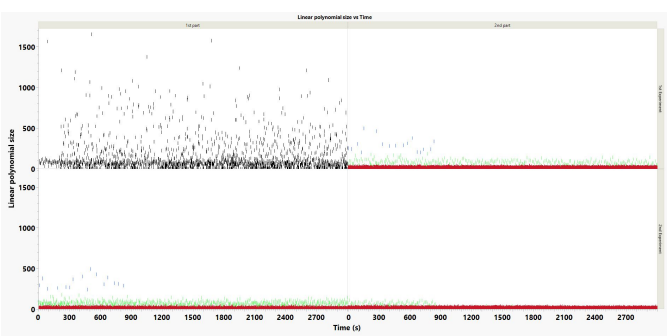

FIGURE 15. **Size of linear polynomials constituting drifts vs Experiments. As resonance frequencies are sampled at a constant time step (every 400ms), the size of a linear polynomial is equivalent to its duration. The *x*-axis is the time and the y-label is the linear polynomial size. The first line of plots represent the landing events for the first experiment, separated according to our recording constraints (Left: data recorded from $[0, 2600]s$, Right: data recorded from $[2600, 4200]s$). The second line of plots represent the landing events for the second experiment, separated according to our recording constraints (Left: data recorded from $[0, 2600]s$, Right: data recorded from $[2600, 4200]s$). The different colors represent the clusters as identified by the K-means method: Red is the first cluster, green is the second cluster and blue the third one. Note that all time are rescaled on the same interval to ease comparisons.**

We now focus on the link between the slopes of the linear polynomials in the first and second resonance frequencies. Under the assumption of continuous adsorption of solvent gas, there is indeed a linear correlation between the slopes of the linear polynomials constituting drifts, as proved in Appendix F. This correlation has a known coefficient that is directly related to NEMS geometry. If the function of the drift sizes over time seems to behave as expected by our modeling, it is crucial to check the expected linear correlation to validate it. Such a correlation is accessible by plotting the slopes of the linear polynomials in the first resonance frequency versus the slopes of the linear polynomials in the second resonance frequency, as shown in Figures 16, 17 and 18.

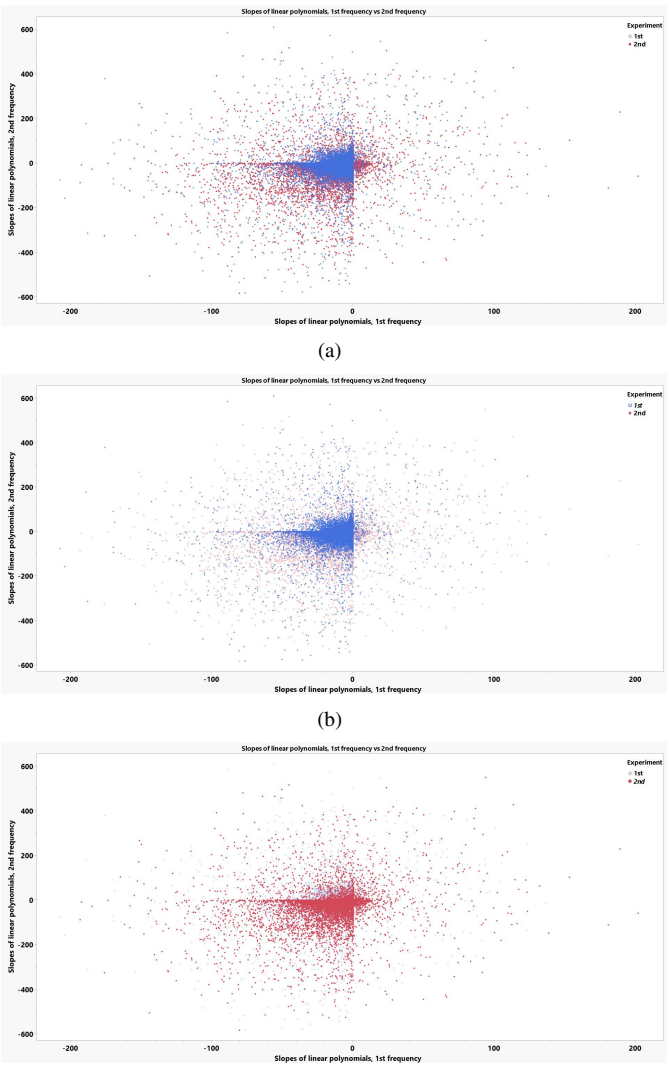

(a)

(b)

(c)

FIGURE 16. **Slopes ratio of linear polynomials. These plots are obtained by selecting the first cluster of the K-means method. This represents the set of the shortest linear polynomials. (a) Data points for both experiments. (b) Data points of first experiment only. (c) Data points of second experiment only.**

It appears there is no linear correlation between the linear polynomials with the shortest sizes. In addition to the visual aspects shown in Figure 16, the different possible correlation factors point towards the absence of linearity. Indeed, if we compute the correlation for each situation represented in Figure 16, we always obtain a correlation coefficient lower than 0.2. Consequently, this type of linear polynomial cannot be

related to the modeling of continuous solvent gas adsorption. More likely, these polynomials represent the residues of the Gaussian noise that have not been entirely eliminated from the frequency traces by the constraints in Equations (4), (5), and (6).

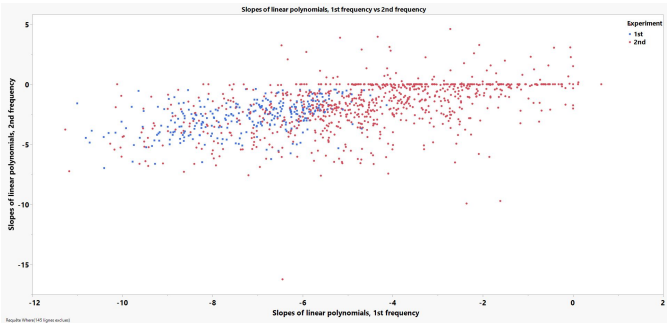

(a)

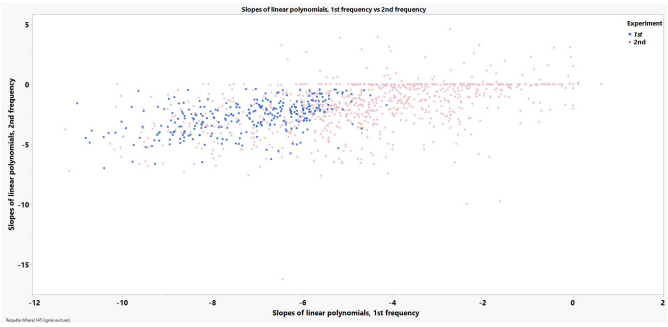

(b)

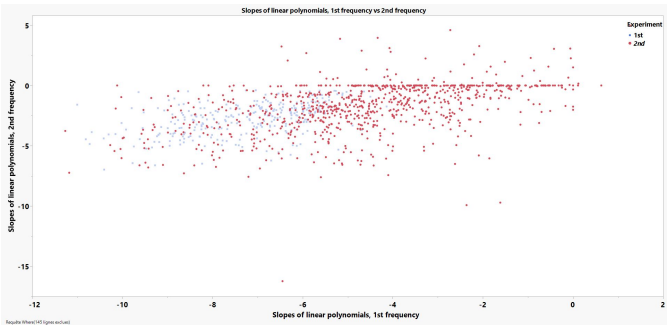

(c)

FIGURE 17. Slopes ratio of linear polynomials. These plots are obtained by selecting the second cluster of the K-means method. This represents the set of linear polynomials with intermediate sizes. (a) Data points for both experiments. (b) Data points of first experiment only. (c) Data points of second experiment only.

The conclusions are similar for the linear polynomials with intermediate sizes. The computations of correlation coefficients reinforce the visual impression from Figure 10, where no linear relations between the slopes of linear polynomials in the first and second resonance frequencies seem to be present. At most, we obtain a correlation coefficient of 0.52 when simultaneously working on data from the first and second experiment. Thus, we cannot associate these linear polynomials with our solvent gas adsorption model. However, we also observe that the data behave slightly differently, depending on the experiment. This may be due to some differences in the experimental conditions; however, there is no clear evidence yet.

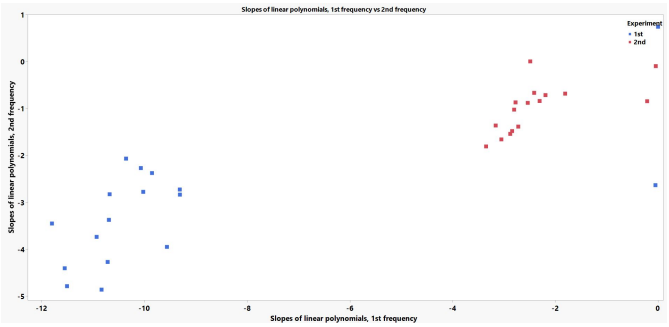

FIGURE 18. Slopes ratio of linear polynomials. These plots are obtained by selecting the third cluster of the K-means method. This represents the set of linear polynomials with the highest sizes.

The situation is slightly more complex with the linear polynomials of highest sizes. First, we observe that there is a clear separation between the data depending on the experiment. This shows that despite a comparable mass distribution, the resonance frequency traces are influenced by some external phenomena. Such a data configuration could be a clue to determine if the experimental conditions are truly equivalent from one experiment to another, or if the state of NEMS changes across experiments (for instance, we could think of a change in the solvent gas affinity, which modifies the adsorption rate due to the NEMS surface state). If we compute the linear correlation for each experiment, we get 0.68 for the first one and 0.63 for the second one. This is still not sufficient to make a positive conclusion for our solvent gas adsorption modeling, but the trend is stronger than that for the other types of linear polynomials. Nevertheless, for this set of linear polynomials, the number of data points for every experiment is low (approximately 15 for each), and may not be high enough to make a relevant decision. Additional experiments are required to obtain a definitive answer. Finally, we also compute a linear regression on these data to compare the obtained slope and intercept to the theoretical ones given by our modeling (which should be equal to 0.602 and 0; see Appendix F). We always obtain either inadequate intercept and/or slope values when comparing them to the expected values. Thus, these results do not validate our continuous deposition modeling; however, the low number of elements in the class of long linear polynomials prevents us from providing a definitive conclusion. Despite the lack of strong evidence towards the proposed model, it is worth noting that our algorithm reveals that the drift behavior varies from one day to another. Just like for the polynomials of intermediate sizes, this could indicate that drifts are influenced by experimental conditions.

REFERENCES

[1] S. Dominguez-Medina, S. Fostner, M. Defoort, M. Sansa, A.-K. Stark, M. Abdul Halim, E. Vernhes, M. Gely, G. Jourdan, T. Alava, P. Boulanger, C. Masselon and S. Hentz, "Neutral mass spectrometry of virus capsids above

100 megadaltons with nanomechanical resonators," *Science*, vol. 362, no. 6417, pp. 918–922, 2018, DOI: 10.1126/science.aat6457

[2] S.-H. Lai, A. Reynaud, N.-N. Zhang, M. Kwak, B. Vysotskyi, S. Dominguez-Medina, T. Fortin, K. Clement, M. Defoort, T.-G. Lee, K. Liu, S. Hentz and C. Masselon, "Characterizing Nanoparticle Mass Distributions Using Charge-Independent Nanoresonator Mass Spectrometry," *The Journal of Physical Chemistry C*, vol. 126, no. 49, pp. 20946–20953, 2022, DOI: 10.1021/acs.jpcc.2c06675

[3] I. Stachiv, Z. Machů, O. Ševeček, Y.-R. Jeng, W.-L. Li, M. Kotoul and J. Prášek "Achievable accuracy of resonating nanomechanical systems for mass sensing of larger analytes in GDa range," *International Journal of Mechanical Sciences*, vol. 224, 2022, DOI: 10.1016/j.ijmecsci.2022.107353

[4] M. S. Hanay, S. Kelber, A. K. Naik, D. chi, S. Hentz, E. C. Bullard, E. Colinet, L. Duraffourg and M. L. Roukes, "Single-protein nanomechanical mass spectrometry in real time," *Nature Nanotechnology*, vol. 7, pp. 602–608, 2012, DOI: 10.1038/nnano.2012.119

[5] A. Bouchaala, A. Nayfeh, N. Jaber and M. I. Younis, "Mass and position determination in MEMS mass sensors: a theoretical and an experimental investigation," *Journal of Micromechanics and Microengineering*, vol. 26, no. 10, 2016, DOI: 10.1088/0960-1317/26/10/105009

[6] E. Sage, "New concept of mass spectrometer based on arrays of resonating nanostructure," Ph.D. dissertation, Université de Grenoble, Grenoble, France, 2016, [Online] Available: https://tel.archives-ouvertes.fr/tel-01178607

[7] R. Perenon, "Traitement de l'information en mode comptage appliqué aux détecteurs spectrométriques," Ph.D. dissertation, Université de Grenoble, Grenoble, France, 2013, [Online] Available: https://tel.archives-ouvertes.fr/tel-00957594/document

[8] K. Clement, "Multi-level characterization of bacteriophage T5 capsids and capsid-like particles using mass spectrometry," Ph.D. dissertation, Université Grenoble Alpes, Grenoble, France, 2021, [Online] Available: https://www.theses.fr/2021GRALV042.pdf

[9] M. Sansa, E. Sage, E. C. Bullard, M. Gély, T. Alava, E. Colinet, A. K. Naik, L. G. Villanueva, L. Duraffourg, M. L. Roukes, G. Jourdan and S. Hentz, "Frequency fluctuations in silicon nanoresonators," *Nature nanotechnology*, vol. 11, pp. 552–558, 2016, DOI: 10.1038/nnano.2016.19

[10] T. Fortin, B. Vysotskyi, M. Defoort, A. Reynaud, S.-H. Lai, S. Dominguez-Medina, K. Clement, V. Çumaku, S. Hentz and C. Masselon, "A Nonlinear Model for Nano-Electro Mechanical Mass Sensing Signals Processing," *IEEE Sensors J.*, vol. 21, no. 19, pp. 21852–21861, 2021, DOI: 10.1109/JSEN.2021.3103713

[11] A. Chambolle and P.-L. Lions, "Image recovery via total variation minimization and related problems," *Numerische Mathematik*, no. 76, pp. 167–188, 1997, DOI: 10.1007/s002110050258

[12] L. I. Rudin, S. Osher and E. Fatemi, "Nonlinear total variation based noise removal algorithms," *Physica D: Nonlinear Phenomena*, vol. 60, no. 1-4, pp. 259–268, 1992, DOI: 10.1016/0167-2789(92)90242-F

[13] A. Reynaud, W. Trzpil, L. Dartiguelongue, V. Çumaku, T. Fortin, M. Sansa, S. Hentz and C. Masselon, "Compact and Modular System Architecture for a Nano-Resonator-Mass Spectrometer," *Frontiers in Chemistry*, vol. 11, 2023, DOI: 10.3389/fchem.2023.1238674

[14] C. Truong, L. Oudre and N. Vayatis, "Selective review of offline change point detection methods," *Signal Processing*, vol. 167, 2020, DOI: 10.1016/j.sigpro.2019.107299

[15] A. Beck and M. Teboulle, "Fast Gradient-Based Algorithms for Constrained Total Variation Image Denoising and Deblurring Problems," *IEEE Trans. Image Process.*, vol. 18, no. 11, pp. 2419–2434, 2009, DOI: 10.1109/TIP.2009.2028250

[16] A. Beck and M. Teboulle, "A Fast Iterative Shrinkage-Thresholding Algorithm for Linear Inverse Problems," *SIAM Journal on Imaging Sciences*, vol. 2, no. 1, pp. 183–202, 2009, DOI: 10.1137/080716542

[17] P. Weiss, L. Blanc-Féraud and G. Aubert, "Efficient Schemes for Total Variation Minimization Under Constraints in Image Processing," *SIAM Journal on Scientific Computing*, vol. 31, no. 3, pp. 2047–2080, 2009, DOI: 10.1137/070696143

[18] Y. Nesterov, *Lecture on Convex Optimization*, 2nd ed., Springer Cham, 2018, DOI: 10.1007/978-3-319-91578-4

[19] Y. Nesterov, "Gradient methods for minimizing composite functions," *Mathematical Programming*, vol. 140, pp. 125–161, 2013, DOI: 10.1007/s10107-012-0629-5

[20] R. Gu and A. Dogandžić, "Projected Nesterov's Proximal-Gradient Algorithm for Sparse Signal Recovery," *IEEE Trans. Signal Process.*, vol. 65, no. 13, pp. 3510–3525, 2017, DOI: 10.1109/TSP.2017.2691661

[21] A. Chambolle, "An algorithm for total variation minimization and applications," *J. Math. Imaging Vis.*, vol. 20, no. 1-2, pp. 89–97, 2004, DOI: 10.1023/B:JMIV.0000011325.36760.1e

[22] A. Langer, "Automated Parameter Selection for Total Variation Minimization in Image Restoration," *J. Math. Imaging Vis*, no. 57, pp. 239–268, 2017, DOI: 10.1007/s10851-016-0676-2

[23] S. Antoine, J.-F. Aujol, Y. Boursier and C. Mélot, "Some proximal methods for Poisson intensity CBCT and PET," *Inverse Problems and Imaging*, vol. 6, no. 4, pp. 565–598, 2012, DOI: 10.3934/ipi.2012.6.565

[24] I. Ekeland and R. Témam, *Convex Analysis and Variational Problems*, Society for Industrial and Applied Mathematics, 1999, DOI: 10.1137/1.9781611971088

[25] R. H. Byrd, P. Lu, J. Noceda and C. Zhu, "A limited memory algorithm for bound constrained optimization," *SIAM Journal on Scientific Computing*, vol. 16, no. 5, pp. 1190–1208, 1995, DOI: 10.1137/0916069

[26] C. Zhu, R. H. Byrd, P. Lu and J. Nocedal, "L-BFGS-B: Fortran subroutines for large-scale bound-constrained optimization," *ACM Transactions on Mathematical Software*, vol. 23, no. 4, pp. 550–560, 1997, DOI: 10.1145/279232.279236

[27] B. L. Milman, "General principles of identification by mass spectrometry,", *TrAC Trends in Analytical Chemistry*, vol. 69, pp. 24–33, 2015, DOI: 10.1016/j.trac.2014.12.009

[28] K. K. Park, H. Lee, M. Kupnik, Ö. Oralkan, J.-P. Ramseyer, H. P. Lang, M. Hegner, C. Gerber and B. T. Khuri-Yakub, "Capacitive micromachined ultrasonic transducer (CMUT) as a chemical sensor for DMMP detection," *Sensors and Actuators B: Chemical*, vol. 160, no. 1, pp. 1120–1127, 2011, DOI: 10.1016/j.snb.2011.09.036

[29] P. W. Hawkes and J. C. H. Spence, *Springer Handbook of Microscopy*, 1st ed., Springer Cham, 2019, DOI: 10.1007/978-3-030-00069-1

[30] B. Voigtländer, *Atomic Force Microscopy*, 2nd ed., Springer Cham, 2019, DOI: 10.1007/978-3-030-13654-3

[31] S. Jeudy, L. Bertaux, J-M. Alempic, A. Lartigue, M. Legendre, L. Belmudes, S. Santini, N. Philippe, L. Beucher, E. G. Biondi, S. Juul, D. J. Turner, Y. Couté, J-M. Claverie and C. Abergel, "Exploration of the propagation of transpovirons within Mimiviridae reveals a unique example of commensalism in the viral world," *ISME J*, vol. 14, pp. 727–739, 2020, DOI: 10.1038/s41396-019-0565-y

[32] J.-M. Claverie and C. Abergel, "Mimivirus and its Virophage," *Annu Rev Genet.*, vol. 43, pp. 49–66, 2009, DOI: 10.1146/annurev-genet-102108-134255

[33] B. La Scola, C. Desnues, I. Pagnier, C. Robert, L. Barrassi, G. Fournous, M. Merchat, M. Suzan-Monti, P. Forterre, E. Koonin and D. Raoult, "The virophage as a unique parasite of the giant mimivirus," *Nature*, vol. 455, pp. 100–104, 2008, DOI: 10.1038/nature07218

[34] X. Zhang, S. Sun, Y. Xiang, J. Wong, T. Klose, D. Raoult and M. G. Rossmann, "Structure of Sputnik, a virophage, at 3.5-Å resolution," *Biophysics and Computational Biology*, vol. 109, no. 45, pp. 18431–18436, 2012, DOI: 10.1073/pnas.121170210

[35] W. Wu and D. Hu and C. Niu and H. Yu and V. Vardhanabhuti and G. Wang, "DRONE: Dual-Domain Residual-based Optimization NEtwork for Sparse-View CT Reconstruction," *IEEE Trans. Med. Imaging*, vol. 40, no. 11, pp. 3002–3014, 2021, DOI: 10.1109/TMI.2021.3078067

[36] W. Wu and Y. Wang and Q. Liu and G. Wang and J. Zhang, "Wavelet-improved Score-based Generative Model for Medical Imaging," *IEEE Trans. Med. Imaging*, DOI: 10.1109/TMI.2023.3325824

THOMAS FORTIN received the master's degree in mathematical engineering from the Université Paris-Sud, Orsay, France, in 2001 and the Ph.D. degree in numerical analysis from Université Pierre et Marie Curie, France, in 2006. From 2007 to 2014, he was a research engineer for the Nuclear Energy Department, CEA, Grenoble, France, and worked on numerical schemes for fluid dynamics. Since 2014, he has worked as a research engineer at the Interdisciplinary Research Institute of Grenoble (IRIG), Grenoble, France, and has focused on signal processing applied to mass spectrometry signals. His research interests include signal processing, numerical analysis, applied mathematics and scientific computing.

ADRIEN REYNAUD obtained his PhD at IFPEN in 2019 where he studied a soot particle microsensor to monitor diesel particle filter loading in thermal engine vehicles. In 2020, he joined CEA as a post-doctoral researcher to work on NEMS-MS apparatus dedicated to viral like particle mass measurements. He is currently working in Oberon Sciences as a junior scientist in aerosol physics instrumentation.

SANDRA JEUDY is a CNRS researcher and currently works at IGS Laboratory, Marseille (France). Her current interest is in the hyper parasitism occurring in *Acanthamoeba castellanii*, involving giant viruses, virophages and transpovirons.

SZU-HSUEH LAI currently works for the Department of Chemistry at National Cheng Kung University, Tainan, Taiwan

VAITSON ÇUMAKU received a bachelor's degree in fundamental Biology in 2018 and a master's degree in Physics, branch Nanobiosciences, in 2020, both from the University Grenoble Alpes. He is currently pursuing his PhD degree, since 2020, in the doctoral school of Chemistry and Life Sciences (EDCSV) at the University Grenoble Alpes, in the branch of Structural Biology and Nanobiosciences.

CHANTAL ABERGEL is a research director at CNRS and is head of the IGS Laboratory, Marseille (France). Her research focuses on the isolation of giant viruses, the functional characterization of the numerous proteins they encode, and their role during their infectious cycles.

SÉBASTIEN HENTZ currently works for CEA LITEN, Grenoble, France.

CHRISTOPHE MASSELON currently works for Interdisciplinary Research Institute of Grenoble (IRIG), Grenoble, France.